Tetrathiafulvalene-amido-2-pyridine-N-oxide as Efficient Charge-Transfer Antenna Ligand for the Sensitization of YbIII Luminescence in a Series of Lanthanide Paramagnetic Coordinat...

ARTICLE *in* CHEMISTRY - A EUROPEAN JOURNAL · OCTOBER 2010

Impact Factor: 5.73 · DOI: 10.1002/chem.201001450 · Source: PubMed

CHEMISTRY
A EUROPEAN JOURNAL

DOI: 10.1002/chem.201001450

Tetrathiafulvalene-amido-2-pyridine-*N*-oxide as Efficient Charge-Transfer Antenna Ligand for the Sensitization of Yb^{III} Luminescence in a Series of Lanthanide Paramagnetic Coordination Complexes

Fabrice Pointillart,[a] Thomas Cauchy,[a] Olivier Maury,[b] Yann Le Gal,[a] Stéphane Golhen,[a] Olivier Cador,[a] and Lahcène Ouahab*[a]

Abstract: The tetrathiafulvalene-amido-2-pyridine-*N*-oxide (**L**) ligand has been employed to coordinate 4f elements. The architecture of the complexes mainly depends on the ionic radii of the lanthanides. Thus, the reaction of **L** in the same experimental protocol leads to three different molecular structure series. Binuclear $[Ln_2(hfac)_5(O_2CPhCl)(\mathbf{L})_3]\cdot 2H_2O$ ($hfac^- =$ 1,1,1,5,5,5-hexafluoroacetylacetonate anion, $O_2CPhCl^- =$ 3-chlorobenzoate anion) and mononuclear $[Ln(hfac)_3(\mathbf{L})_2]$ complexes were obtained by using rare-earth ions with either large ($Ln^{III} =$ Pr, Gd) or small ($Ln^{III} =$ Y, Yb) ionic radius, respectively, whereas the use of Tb^{III} that possesses an intermediate ionic radius led to the formation of a binuclear complex of formula $[Tb_2(hfac)_4(O_2CPhCl)_2(\mathbf{L})_2]$. Antiferromagnetic interactions have been observed in the three dinuclear compounds by using an extended empirical method. Photophysical properties of the coordination complexes have been studied by solid-state absorption spectroscopy, whereas time-dependent density functional theory (TD-DFT) calculations have been carried out on the diamagnetic Y^{III} derivative to build a molecular orbital diagram and to reproduce the absorption spectrum. For the $[Yb(hfac)_3(\mathbf{L})_2]$ complex, the excitation at 19600 cm^{-1} of the HOMO→LUMO+1/LUMO+2 charge-transfer transition induces both line-shape emissions in the near-IR spectral range assigned to the $^2F_{5/2} \rightarrow {}^2F_{7/2}$ (9860 cm^{-1}) ytterbium-centered transition and a residual charge-transfer emission around 13150 cm^{-1}. An efficient antenna effect that proceeds through energy transfer from the singlet excited state of the tetrathiafulvalene-amido-2-pyridine-*N*-oxide chromophore is evidence of the Yb^{III} sensitization.

Keywords: density functional calculations · lanthanides · luminescence · magnetic properties · tetrathiafulvalene

Introduction

Research of new multifunctional materials based on tetrathiafulvalene (TTF) has emerged in the last decade.[1] To elaborate such materials,[2] two strategies are usually investigated: the through-space and the covalent approaches. The latter one appears as a promising alternative to obtain strong interactions between the metal and the redox-active ligands.[3] Such an approach can be applied to the elaboration of π–f systems, which are very scarce.[4] In this context, trivalent lanthanides present many advantages. Indeed, their large spins and pronounced spin–orbit coupling, in particular for Dy^{III} and Tb^{III} ions, result in strong Ising-type magnetic anisotropy[5] that leads to good candidates for obtaining single-molecule magnets (SMMs) and single-chain magnets (SCMs).[6] In addition, the lanthanides have been widely studied for their specific luminescence properties (emission lines that range from the visible to the near-infrared spec-

[a] Dr. F. Pointillart, Dr. T. Cauchy, Y. Le Gal, Dr. S. Golhen, Dr. O. Cador, Dr. L. Ouahab
Sciences Chimiques de Rennes, UMR 6226 CNRS
Université de Rennes 1, 263 Avenue du Général Leclerc
35042 Rennes Cedex (France)
Fax: (+33) 223236840
E-mail: Lahcene.ouahab@univ-rennes1.fr

[b] Dr. O. Maury
Laboratoire de Chimie de l'ENS-LYON-UMR 5182
46 Allée d'Italie, 69364 Lyon Cedex 07 (France)

Supporting information for this article is available on the WWW under http://dx.doi.org/10.1002/chem.201001450. ORTEP views for **1** (Figure S1), and **4** (Figure S2); cyclic voltammetry for **L** and complexes **1**–**5** (Figure S3); thermal analysis for **4** (Figure S4); first magnetization for **1** and **3** (Figure S5 and S6); solid-state UV-visible absorption spectra for **2** and **4** (Figure S7); solution UV-visible absorption spectra for **L** (Figure S8); and all the TD-DFT data for **L** and **4** (Tables S1 and S2).

trum, microsecond–millisecond luminescence lifetimes to allow time-gated detection, and large pseudo-Stokes shifts considering a ligand excitation).[7] Owing to the weak absorption of the forbidden f–f transitions, the rare-earth emission is usually sensitized by organic antenna chromophores that strongly absorb the UV-visible light and whose triplet state matches the accepting level of the lanthanide ion so that an efficient energy transfer occurs.[8] According to this classical strategy, highly stable complexes associating a chromophore to a tris-β-diketonate lanthanide platform have been designed leading to potential applications in chelate lasers[9] or efficient organic light emitting diodes (OLEDs),[10] and polymer light emitting diodes (PLEDs).[11] Nowadays a great research endeavor is devoted to the sensitization of near-infrared (NIR) luminescent lanthanides (Nd^{III}, Yb^{III}, Er^{III}, and to a lesser extend Ho^{III} and Pr^{III}) for potential applications in telecommunication or in vivo bioimaging.[12] At the same time, an actual challenge is to shift the excitation wavelength from the UV to the visible spectral range to limit the photodamage of biological tissues and, from a practical point of view, to allow the use of cheap excitation source and glass optics. Such purpose requires the development of alternative photophysical sensitization processes to the classical "triplet state"-mediated one. In this context, three main sensitization strategies have been explored: 1) direct from a charge-transfer (ILCT) state,[13] 2) by means of a triplet metal-to-ligand charge-transfer (^{3}MLCT) state of various transition metals (Ru^{II}, Os^{II}, Ir^{II}, Pt^{II}, Re^{I}),[14] and 3) using a nonlinear multiphoton excitation (from two- to four-photon excitation).[15]

The combination and coexistence of both luminescence and magnetism in the same molecule is a new challenge in the study of SMMs and SCMs.[16] In fact, recently, efforts have been made to study SMMs at the single-molecule level by placing them on surfaces.[17] Nevertheless, it can often be difficult to determine the exact position or dispersion of species (SMMs, SCMs, and also more simply paramagnetic molecules) deposited on surfaces. Furthermore, below the blocking temperature T_B, and if the magnetic moment of a SMM or SCM is coupled with the photoexcited states of photoluminescent ligands, this may provide a new tool for studying the fundamental quantum behavior exhibited by SMMs and SCMs on a 10^{-9}–10^{-12} s timescale.

The aim of this work is the elaboration of lanthanide-based coordination complexes involving redox-active functionalized TTF as organic ligands, which also play the role of antenna for the sensitization of NIR emitters.[18,4g] In this way, we have reported redox-active tetrathiafulvalene-amido-2-pyrimidine-1-oxide (TTF-CONH-2-Pym-1-oxide) that efficiently coordinates a lanthanide ion through the NO bond and gives the first published crystal structures of a coordination complex involving a TTF derivative and lanthanide.[19,4g] Very recently we have studied the coordination ability and the absorption properties of a new redox-active tetrathiafulvalene-amido-2-pyridine-*N*-oxide ligand (**L**) with 3d ions.[20] We now extend our investigation to the rare-earth series.

In the following, we report the reactions between the ligand **L** and a series of $Ln(hfac)_3{\cdot}x\,H_2O$ precursors (Ln^{III} = Pr, Gd, Tb, Y, and Yb) leading to the formation of five coordinating complexes of three structural families: $[Ln_2(hfac)_5(O_2CPhCl)(L)_3]{\cdot}2\,H_2O$ (Ln^{III} = Pr (**1**) and Gd (**2**)), $[Tb_2(hfac)_4(O_2CPhCl)_2(L)_2]$ (**3**), and $[Ln(hfac)_3(L)_2]$ (Ln^{III} = Y (**4**) and Yb (**5**)). This series of lanthanides includes magnetic isotropy (Gd^{III}) and Ising-type anisotropy (Tb^{III}), NIR luminescence (Pr^{III} and Yb^{III}), and a diamagnetic model (Y^{III}) for computational calculations. All the complexes have been characterized by single-crystal X-ray diffraction, IR spectroscopy, solid-state UV-visible absorption spectroscopy, and magnetic measurements (superconducting quantum interference device (SQUID)). The UV-visible absorption spectroscopy has been carried out on the basis of theoretical simulations of the absorption spectrum of **4** and its luminescence.

Results and Discussion

Synthesis: The 4f electrons are generally described as non-polarizable core electrons.[21,22] The experimental observations of the ligand-field effect by means of luminescence[15a,23] or NMR spectroscopy[24] and the recent discovery of the direct contribution of f electrons to the nonlinear optical activity[8,25] brought into question the claimed inertness of the 4f electrons and led to a reassessment of their description by theoretical calculations.[26] The ionic-radius contraction is well known for the lanthanides if the reactivity along the 4f series is homogeneous.[27] So from the same experimental protocol, different molecular compounds can be expected using different lanthanides.

The interactions between the Ln^{III} ions and the ligands are electrostatic, thus such metal ions are considered as strong Lewis acids (oxophile ions).[28] Tetrathiafulvalene-amido-2-pyridine-*N*-oxide (**L**) is then a good candidate to fill the coordination sphere of lanthanides.

The reactivity of this ligand with different Ln^{III} ions (Ln = Pr, Gd, Tb, Y, and Yb) is explored by taking into account the following protocol: 3-chlorobenzoic acid (1 equiv) and donor **L** (2.5 equiv) are added to the noncoordinating CH_2Cl_2 solvent in the presence of the $Ln(hfac)_3{\cdot}2\,H_2O$ (1 equiv) precursor (Scheme 1). 3-Chlorobenzoic acid is added because it is soluble in noncoordinating solvent and it may connect the $Ln(hfac)_3$ unit together to increase the nu-

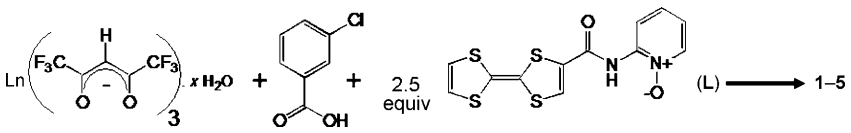

Scheme 1. Synthesis of $[Ln_2(hfac)_5(O_2CPhCl)(L)_3]{\cdot}2\,H_2O$ (Ln = Pr (**1**) and Gd (**2**)), $[Tb_2(hfac)_4(O_2CPhCl)_2(L)_2]$ (**3**), and $[Ln(hfac)_3(L)_2]$ (Ln = Y (**4**) and Yb (**5**)).

clearity. All the compounds are isolated as single crystals by slow diffusion of *n*-hexane in the dark. Different compounds are obtained, depending of the ionic radius of the Ln^{III} ions. In this way, the largest lanthanides give the $[Ln_2(hfac)_5(O_2CPhCl)(\mathbf{L})_3]\cdot 2H_2O$ complexes (Ln = Pr^{III} (**1**) and Gd^{III} (**2**)), the smallest ones give the $[Ln(hfac)_3(\mathbf{L})_2]$ complexes (Ln = Y^{III} (**4**) and Yb^{III} (**5**)), and finally the intermediate-sized Tb^{III} ion leads to the formation of the $[Tb_2(hfac)_4(O_2CPhCl)_2(\mathbf{L})_2]$ (**3**) complex.

Crystal-structure analysis

$[Ln_2(hfac)_5(O_2CPhCl)(L)_3]\cdot 2H_2O$ (Ln = Pr (1) and Gd (2)): The two compounds are isostructural, therefore, the structure of **2** is described and the corresponding values for **1** are given in square brackets for comparison. The structure analysis is performed on the best-resolved structure. Both compounds crystallize in the monoclinic $P2_1/c$ (no. 14) space group (Table 1). The asymmetric unit is composed of one $Gd(hfac)_3$ [$Pr(hfac)_3$] and one $Gd(hfac)_2$ [$Pr(hfac)_2$] unit linked by two bridging μ_2-**L** ligands (O2 and O4) and one bridging $\mu_2(\eta_1,\eta_2)$-3-chlorobenzoate anion (O11) (Figure 1) [Figure S1 in the Supporting Information]. The presence of an anionic bridge explains the loss of one $hfac^-$ ligand in the coordination sphere of Gd2 [Pr2]. Two water solvent molecules of crystallization are found. The coordination sphere of Gd1 [Pr1] is filled by a terminal **L** ligand (O14). The metal centers are nine-coordinated and the Ln–O distances range from 2.362(5)[2.405(6)] to 2.592(4)[2.653(6)] Å (Table 2). The donors **L** are coordinated through the N–O group and the Gd-O-N angles take a mean value of 127.9(3)[128.3(5)]°, which is close to the values observed for $[Gd(hfac)_3(TTF\text{-}CONH\text{-}2\text{-}pym\text{-}1\text{-}oxide)_3]\cdot CH_2Cl_2\cdot 0.5\,C_6H_{14}$[19] but lower than the usual angle value (about 150°) for Ln-O-$N_{nitronyl-nitroxide}$.[29] The arrangements of the linked ligands lead to coordination polyhedra that can be described like distorted 4,4,4-tricapped trigonal prisms with fourteen triangular faces.[30] The symmetry of the coordination polyhedra is close to D_{3h}. In the tricapped trigonal prismatic polyhedron

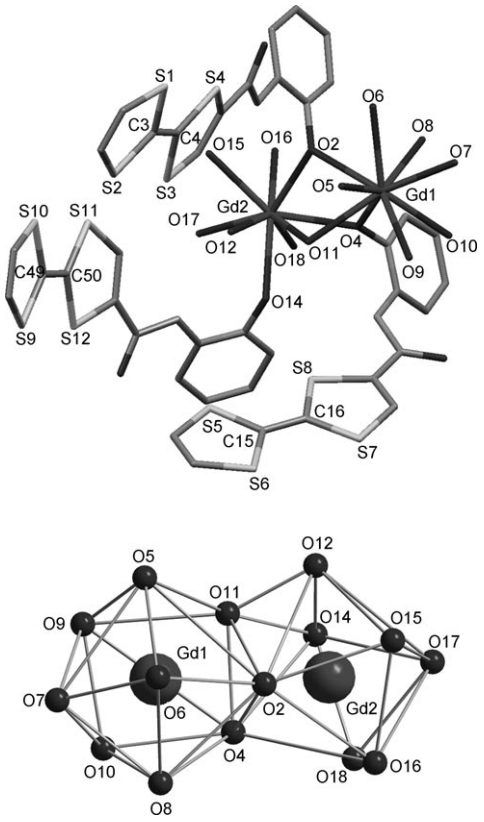

Figure 1. Molecular structure of **2** with coordination polyhedra around Gd^{III}. Only the first neighbor atoms of the metal atoms and ligands **L** are shown for clarity.

Table 1. X-ray crystallographic data.

	1	**2**	**3**	**4**	**5**
formula	$C_{68}H_{37}Cl_1F_{30}N_6O_{20}S_{12}Pr_2$	$C_{68}H_{37}Cl_1F_{30}N_6O_{20}S_{12}Gd_2$	$C_{58}H_{32}Cl_2F_{24}N_4O_{18}S_8Tb_2$	$C_{39}H_{20}F_{18}N_4O_{10}S_8Y$	$C_{39}H_{20}F_{18}N_4O_{10}S_8Yb$
M_r [g mol^{-1}]	2528.3	2561.0	2172.8	1390.9	1475.0
crystal system	monoclinic	monoclinic	triclinic	triclinic	triclinic
space group	$P21/c$ (no. 14)	$P21/c$ (no. 14)	$P\bar{1}$ (no. 2)	$P\bar{1}$ (no. 2)	$P\bar{1}$ (no. 2)
a [Å]	25.6186(10)	25.479(5)	11.179(5)	12.640(5)	12.622(5)
b [Å]	15.3139(6)	15.263(5)	13.679(5)	13.257(5)	13.242(5)
c [Å]	25.7264(7)	25.646(5)	14.239(5)	16.673(5)	16.629(5)
α [°]	–	–	105.716(5)	105.694(5)	105.573(5)
β [°]	109.495(2)	109.413(5)	104.106(5)	95.189(5)	95.088(5)
γ [°]	–	–	101.740(5)	91.871(5)	91.936(5)
V [Å^3]	9514.4(6)	9406(4)	1946.3(13)	2673.9(17)	2662.0(17)
Z	4	4	2	2	2
T [K]	293(2)	293(2)	293(2)	293(2)	293(2)
diffraction reflection [°]	$5.00 \le 2\theta \le 50.68$	$4.18 \le 2\theta \le 54.22$	$3.14 \le 2\theta \le 55.04$	$5.88 \le 2\theta \le 51.38$	$2.56 \le 2\theta \le 61.16$
ρ_{calcd} [g cm^{-3}]	1.766	1.787	1.855	1.728	1.840
μ [mm^{-1}]	1.429	1.445	2.209	1.522	2.190
no. of reflns	33147	37437	16115	15335	25658
independent reflns	17206	20461	8958	9523	16175
$F_o^2 > 2\sigma(F_o)^2$	9283	13359	7074	6282	10247
no. of variables	1252	1252	551	785	749
R_{int}, R_1, wR_2	0.0920, 0.0708, 0.1314	0.0399, 0.0554, 0.1251	0.0280, 0.0585, 0.1505	0.0374, 0.556, 0.1370	0.0352, 0.573, 0.1413

Table 2. Selected bond lengths [Å] and angles [°] for **1** and **2**.

	1 (Ln = Pr)	**2** (Ln = Gd)
Ln1–O2	2.563(5)	2.488(4)
Ln1–O4	2.639(6)	2.571(4)
Ln1–O5	2.426(6)	2.370(4)
Ln1–O6	2.525(7)	2.493(5)
Ln1–O7	2.426(7)	2.362(5)
Ln1–O8	2.451(6)	2.382(4)
Ln1–O9	2.460(7)	2.404(4)
Ln1–O10	2.484(6)	2.438(4)
Ln1–O11	2.509(6)	2.446(4)
Ln2–O2	2.504(6)	2.441(4)
Ln2–O4	2.484(6)	2.423(4)
Ln2–O11	2.653(6)	2.592(4)
Ln2–O12	2.524(6)	2.452(4)
Ln2–O14	2.405(6)	2.363(4)
Ln2–O15	2.463(6)	2.433(4)
Ln2–O16	2.422(7)	2.362(5)
Ln2–O17	2.436(8)	2.383(5)
Ln2–O18	2.491(8)	2.431(5)
C3–C4	1.352(12)	1.344(9)
C15–C16	1.346(14)	1.338(9)
C49–C50	1.324(19)	1.347(12)
Ln1–Ln2	4.017(1)	3.920(1)
Ln1-O2-N2	126.4(5)	125.9(3)
Ln1-O4-N4	127.2(5)	127.2(3)
Ln2-O2-N2	125.5(5)	125.3(3)
Ln2-O4-N4	129.6(5)	129.4(3)
Ln2-O14-N6	132.6(6)	131.9(4)
Ln1-O2-Ln2	104.89(18)	105.37(13)
Ln1-O4-Ln2	103.23(18)	103.38(13)
Ln1-O11-Ln2	102.14(19)	102.14(13)
ϕ1	43.5(3)	43.6(2)
ϕ2	58.0(3)	57.4(2)
ϕ3	49.3(4)	49.3(2)

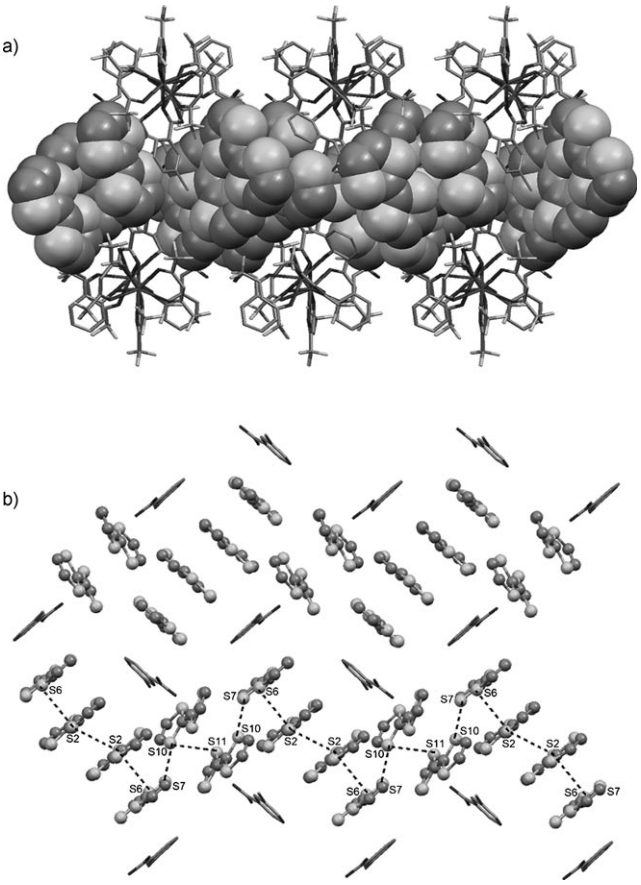

Figure 2. a) Crystal packing of **2** showing the inorganic (capped sticks) and the TTF cores (space-filled) of the organic networks. b) Crystalline arrangement of the TTF fragments and 3-chlorobenzoate anions with the intermolecular S···S contacts highlighted [Å]: S10···S11 = 3.691(4), S2···S2 = 3.719(4), S7···S10 = 3.726(5), and S2···S6 = 3.825(4).

of Gd1 [Pr1], the trigonal faces are formed by atoms O2, O5, O11 and O7, O8, O10, respectively, while the O4, O6, and O9 atoms cap the three quadrilateral faces of the trigonal prism. The dihedral angle between the trigonal planes is 21.2(2)[19.8]°. In the case of Gd2 [Pr2], the trigonal faces are formed by atoms O2, O4, O16 and O12, O14, O17, respectively, while the O11, O15, and O18 atoms cap the three quadrilateral faces of the trigonal prism. The dihedral angle between the trigonal planes is 3.2(2)[3.8(2)]°.

The intramolecular distance between lanthanide ions is 3.920(1)[4.017(1)] Å that is closed to the distance found for a structure involving a similar Ln–Ln skeleton.[31] The TTF cores are almost planar, and the central C=C bond lengths (C3–C4 = (1.344(9)[1.352(13)], C15–C16 = 1.338(9)-[1.346(14)], and C49–C50 = 1.347(12)[1.324(19)] Å) attest that the donors are neutral. ϕ1, ϕ2, and ϕ3 torsion angles are, respectively, defined as the angle between the planes involving the four sulfur atoms of the TTF core and the corresponding pyridine moiety. The large values of ϕ (ϕ1, 43.6(2)-[43.5(3)]°; ϕ2, 57.4(2)[58.0(3)]°; ϕ3, 49.3(2)[49.3(4)]°) demonstrate the flexibility of the amido bridge (Table 2). The flexibility and the disposition of the donors (all the donors are on the same side of the molecule), optimize the formation of two segregated inorganic and organic networks (Figure 2a) with good π–π stacking between the TTF fragments (Figure 2b). The inorganic network is formed by the Ln1-$(hfac)_3$ and Ln2$(hfac)_2$ moieties, whereas the organic network is formed by the donors **L** and the 3-chlorobenzoate anions. The latter is composed of dimers and tetramers of **L** (Figure 2b). The tetramers are sandwiched by 3-chlorobenzoate anions that performed intramolecular π–π interactions with both extremities of the tetramer of **L**. It is worth noting that original intramolecular S···S contacts take place between the sulfur atoms S2···S10 = 3.681(4)[3.675(7)] Å and S3···S11 = 3.683(4)[3.693(6)] Å. Several intermolecular S···S contacts in the range of the sum of the van der Waals radii are observed forming a one-dimensional packing reminiscent of organic donors along the *b* axis (Figure 2b).

$[Tb_2(hfac)_4(O_2CPhCl)_2(L)_2]$ (3): This compound crystallizes in the triclinic $P\bar{1}$ (no. 2) space group (Table 1). The structure consists of a centrosymmetric dimetallic unit made of two terbium ions in a distorted dodecahedral oxygenated coordination sphere (Figure 3); the coordination sphere is made up of eight oxygen atoms arising from two bis-chelate $hfac^-$ anions, one terminal ligand **L**, one water molecule, and two 3-chlorobenzoate anions. The coordination poly-

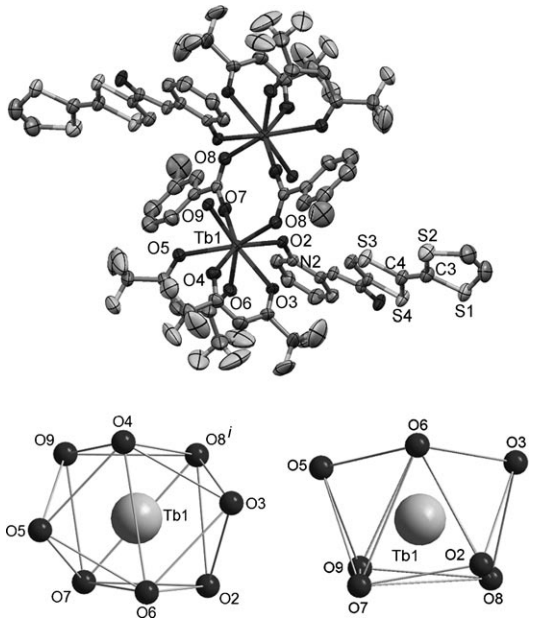

Figure 3. Ortep view of the centrosymmetric unit in **3** with coordination polyhedra around Tb^{III}. Thermal ellipsoids are drawn at 30% probability. Hydrogen atoms are omitted for clarity.

hedron has an almost D_{2d} symmetry. The two {Tb(hfac)$_2$(H$_2$O)(**L**)} units are linked by two bridging $\mu_2(\eta_1,\eta_1)$-3-chlorobenzoate anions (O7, O8^i; Figure 3). As observed in the structures of **1** and **2**, the presence of an anionic bridge explains the loss of one $hfac^-$ ligand in the coordination sphere of Tb1. The Tb–O bond lengths range from 2.304(4) to 2.450(4) Å (Table 3). The donor **L** is coordinated through the N–O group and the Tb1-O2-N2 angle of 131.3(3)° is close to those observed for **1** and **2** but lower than the usual angle value (about 150°) for Ln-O-Nn$_{nitronyl-nitroxide}$.[29] A regular dodecahedron is characterized by four equivalent dihedral angles with a value of 29.5°.[32] In the present case, the distortion of the dodecahedron can be evaluated from the values of its dihedral angles of 18.5(2), 23.0(2), 35.4(2), and 33.8(2)°. The two terbium ions are separated by an intramolecular distance equal to 4.828(2) Å. The central C3–C4 bond length of the TTF fragment (1.327(9) Å) confirms the neutral form of the donor **L**. The neutral ligand **L** in **3** takes a more classical configuration with $\phi 1$ equal to 17.1(2)°, which is much lower than in **1** and **2**. Moreover, the TTF fragment is not planar anymore as usually observed for neutral TTF derivatives. As described previously, the coordination sphere of Tb^{III} is completed by a water molecule that

Table 3. Selected bond lengths [Å] and angles [°] for **3**.

Tb1–O2	2.379(4)	Tb1–O8	2.350(4)
Tb1–O3	2.444(4)	Tb1–O9	2.375(4)
Tb1–O4	2.343(4)	C3–C4	1.327(9)
Tb1–O5	2.450(4)	Tb1-O2-N2	131.3(3)
Tb1–O6	2.344(4)	Tb1–Tb1^i	4.828(2)
Tb1–O7	2.304(4)	$\phi 1$	17.1(2)

plays an important role in the cohesion of the dinuclear complex and its crystal packing. In fact, this water molecule participates in intramolecular (O9···O2^i = 2.808(6) Å) and intermolecular (O9···O1^i = 2.811(7) Å and O9···S4^i = 3.304(5) Å) hydrogen bonds. Each ligand **L** of the dinuclear complex **3** is "head-to-tail" stacked with the neighbor donor (Figure 4a). The two "head-to-tail" stacked donors formed

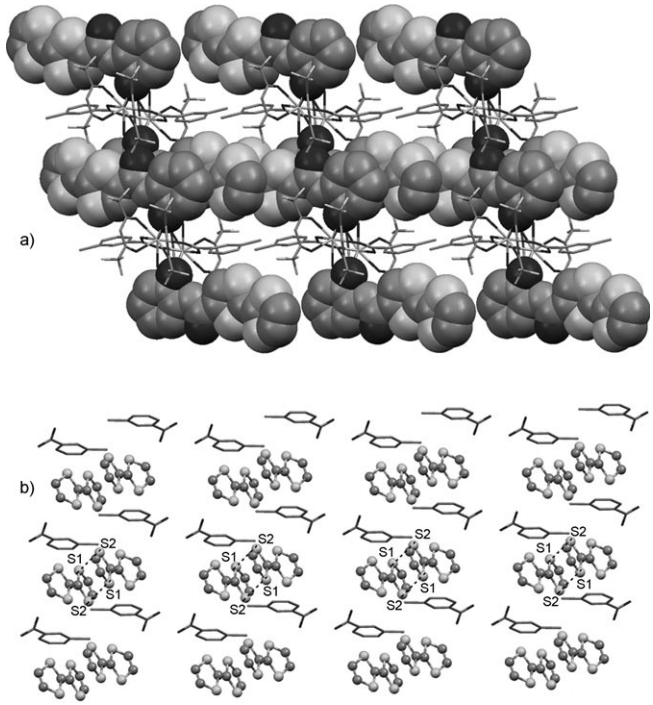

Figure 4. a) Crystal packing of **3** showing the inorganic (capped sticks) and the ligands **L** (space-filled) of the organic networks. b) Crystalline arrangement of the TTF fragments and 3-chlorobenzoate anions with the intermolecular S···S contacts highlighted [Å]: S1···S2 = 3.851(3) Å.

dimers with another TTF derivative through S1···S2 contacts (3.851(3) Å) and a one-dimensional organic chain ran along the *c* axis (Figure 4a). The inorganic network includes the [{Tb(hfac)$_2$(μ-3-chlorobenzoate)}$_2$] units. The arrangement of the dimers and the 3-chlorobenzoate in the crystal structure of **3** is depicted in Figure 4b. The experimental conditions and the donor **L** are the same in the formation of dinuclear complexes **1** to **3**. By taking into account that the reactivity of all the lanthanides is similar, the change of molecular structure is driven by the smaller ionic radius of Tb^{III} relative to that of Pr^{III} and Gd^{III}.

[Ln(hfac)$_3$(L)$_2$] (Ln = Y (4) and Yb (5)): These two compounds are isostructural, therefore, the structure of **5** is described and the respective values for **4** are given in square brackets for comparison. Compound **5** crystallizes in the $P\bar{1}$ (no. 2) triclinic space group (Table 1). An ORTEP view of the asymmetric unit is given in Figure 5 [Figure S2 in the Supporting Information]. This unit is composed of one Yb^{III} metal center linked to eight oxygen atoms coming from

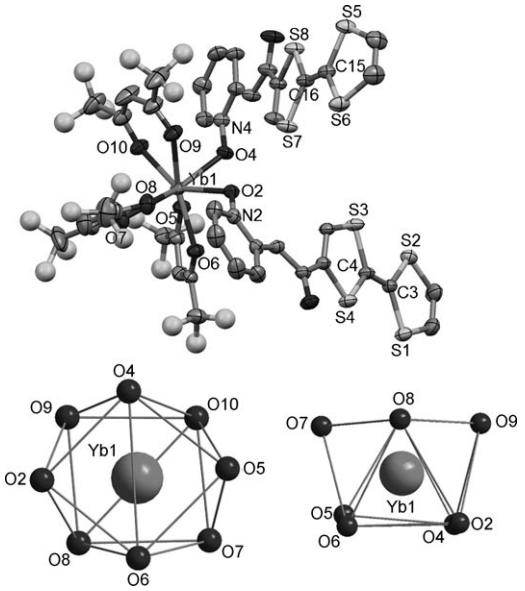

Figure 5. Ortep view of the asymmetric unit in **5** with coordination polyhedra around Yb^{III}. Thermal ellipsoids are drawn at 30% probability. Hydrogen atoms and thermal ellipsoids for fluorine atoms are omitted for clarity.

three bis-chelate hfac$^-$ anions and two terminal **L** donors. The coordination sphere around Ln^{III} can be described as distorted square antiprism polyhedra. The square faces are delimited by atoms O2, O4, O5, O6 and O7, O8, O9, O10, respectively, with the dihedral angle between the corresponding planes being 2.7(1)°. A regular square antiprism polyhedron is characterized by the four ideal dihedral angles taking the following values: 0, 0, 52.4, and 52.4°.[32] In the cases of the mononuclear complexes **4** and **5**, these values have been calculated to be 8.3(2)[8.3(2)], 8.9(2)-[9.4(1)], 56.8(2)[52.9(2)], and 55.7(2)[56.2(1)]°. The 3-chlorobenzoate anion was not found in the structure. The Ln–O bond lengths range from 2.267(4)[2.285(3)] to 2.364(4)-[2.391(4)] Å (Table 4). The donors **L** are coordinated through the N–O group and the Yb1-O2-N2 and Yb1-O4-N4 angles take the values of 122.2(3)[121.9(3)] and 127.2(3)-[128.1(3)] Å. These values are in the same range as those for the dinuclear complexes **1**–**3** (Table 4). Both coordinated **L** are in a *cis* conformation, and they form an angle of 71.8(4)-[72.2(3)]° due to steric effects. The perpendicular arrangement minimizes the steric hindrance of the donors **L**. The central C=C bond length of the TTF fragment (C3–C4 = 1.328(8)[1.336(7)] and C15–C16 = 1.347(7)[1.342(7)] Å) confirms the neutral form of the donor **L**. The torsion angles ϕ1 and ϕ2 are found to be 19.7(1)[18.9(1)] and 6.5(1)[6.8(1)]° and they are comparable with that found for **3**. The inversion center generates two dimers of donors **L** in which the shortest contacts between sulfur atoms are S1···S3 = 3.833(3)[3.838(2)] Å and S5···S6 = 3.724(3)[3.740(3)] Å. Nevertheless, the shortest S···S contacts are S3···S8 = 3.465(2)-[3.463(2)] and S1···S7 = 3.578(2) [3.586(2)] Å. These interactions can be defined as lateral contacts and they are shorter than those observed in the dinuclear complexes and the sum of the van der Waals radii. The intradimers and lateral S···S contacts lead to the formation of a bidimensional organic layer, whereas the Ln(hfac)$_3$ units, constituting the inorganic network, are localized between the organic network (Figure 6a). As observed for **3** relative to **1** and **2**, the decrease of the ionic radius leads to drastic structural changes. The biggest lanthanide ions led to dinuclear complexes including terminal and bridging donors **L** and the 3-chlorobenzoate anion, whereas the smallest ones led to the formation of mononuclear complexes in which terminal donors **L** are observed without the insertion of 3-chlorobenzoate. The Tb^{III}

Table 4. Selected bond lengths [Å] and angles [°] for **4** and **5**.

	4 (Ln = Y)	**5** (Ln = Yb)
Ln1–O2	2.384(3)	2.360(3)
Ln1–O4	2.285(3)	2.267(4)
Ln1–O5	2.352(4)	2.328(4)
Ln1–O6	2.322(3)	2.298(4)
Ln1–O7	2.313(4)	2.358(4)
Ln1–O8	2.364(4)	2.283(5)
Ln1–O9	2.312(4)	2.364(4)
Ln1–O10	2.391(4)	2.278(4)
C3–C4	1.336(7)	1.328(8)
C15–C16	1.342(7)	1.347(7)
Ln1-O2-N2	121.9(3)	122.2(3)
Ln1-O4-N4	128.1(3)	127.2(3)
ϕ1	18.9(1)	19.7(1)
ϕ2	6.8(1)	6.5(1)

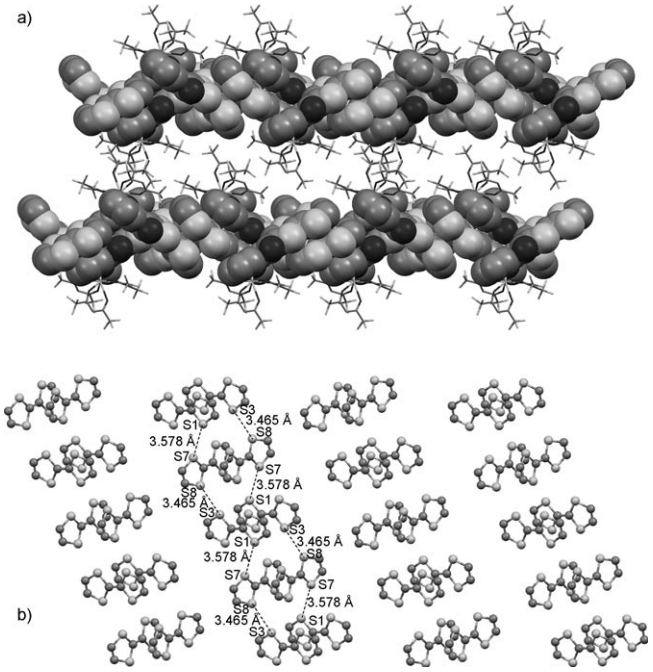

Figure 6. a) Crystal packing of **5** showing the inorganic (capped sticks) and the ligands **L** (space-filled) of the organic networks. b) Crystalline arrangement of the TTF fragments with the intermolecular short S···S contacts highlighted [Å]: S3···S8 = 3.465(3) and S1···S7 = 3.578(3).

ion seems to be the intermediate case between the $[Ln_2(hfac)_5(O_2CPhCl)(\mathbf{L})_3]\cdot 2H_2O$ and $[Ln(hfac)_3(\mathbf{L})_2]$ families of molecular complexes.

Electrochemical properties: The redox properties of **L** and the related complexes were investigated by cyclic voltammetry and the values of the oxidation potentials are listed in Table 5. The measurements have been performed on solutions of the complexes in acetonitrile (CH_3CN) for solubility reasons rather than CH_2Cl_2. The complexes are stable for a few minutes in CH_3CN and their stability has been checked by a change of color. The cyclic votammograms for **1**–**5** show two monoelectronic oxidations at about 0.46 and 0.82 V corresponding to the formation of a radical cation and a dicationic TTF fragment, respectively (Figure S3 in the Supporting Information). No duplication of the oxidation waves is observed, thus signifying that the oxidation and the reduction are simultaneous for all the donors of a complex. Oxidation potentials are shifted to higher positive values relative to the parent TTF due to partial electron transfer from the donor (TTF) to the acceptor moiety. A weak irreversible reduction wave is observed at 0.17 V for the complexes. It may correspond to the reduction of a small part of the pyridine-*N*-oxide moiety in pyridine but no similar behavior has been observed for the precursor 2-aminopyridine-*N*-oxide or for the free ligand **L**. Almost the same oxidation potentials are observed in free and coordinated donors due to the expected weak electronic communication through the nonconjugated amido bridge.[3f] Nevertheless, the electrochemical properties attest to the redox activity of **L** in the complexes and they have the required redox properties to play a good role as molecular precursors for lanthanide-based conducting magnets.

Table 5. Oxidation potentials (V vs. SCE, nBu$_4$NPF$_6$, 0.1 M in acetonitrile at 100 mV s^{-1}) of complexes **1**–**5**.

Compound	$E^1_{1/2}$	$E^2_{1/2}$	E^3
L	0.467	0.818	–
1	0.455	0.821	0.168
2	0.455	0.824	0.164
3	0.440	0.820	0.168
4	0.476	0.828	0.168
5	0.465	0.819	0.176

Thermal analyses: The thermogravimetric analysis of **4** and **5** were performed between 20 and 400 °C. The thermal behavior of both compounds is similar; the results for **4** are given in Figure S4 in the Supporting Information. A single-step weight loss occurs in the range 215–315 °C. The weight loss is equal to 46 % of the total weight of complex **4**, which corresponds to the decoordination of both ligands **L** (theoretical weight loss is 48.9 %). In any case, the $[Ln(hfac)_3(\mathbf{L})_2]$ (Ln = Y and Yb) complexes involving the tetrathiavulvalene-amido-2-pyridine-*N*-oxide as ligand are thermally stable up to 215 °C. The great thermal stability of these compounds is a first step to perform good-quality thin films by vacuum evaporation.[31]

Magnetic properties: The determination of the nature of the exchange interaction in the lanthanide-based complexes is more difficult than in the case of the 3d elements. In the case of 4f ions, the first excited multiplet is separated by more than 1000 cm^{-1} from the ground multiplet.[33] The latter is split in Stark sublevels under the influence of a crystal field.[34] The crystal-field effects are of the order of 100 cm^{-1} for lanthanides. When the temperature decreases, the depopulation of these sublevels leads to a deviation from the Curie law in the absence of any exchange interaction. The $\chi_M T$ product can be written $\chi_M T = \chi_{Ln} T + J$, in which J is the exchange-interaction value between the Ln^{III} ion and the other paramagnetic center. Thus the nature of the magnetic exchange interaction cannot be determined from the shape of the experimental $\chi_M T$ curve. An empirical method has already been used to determine the nature of the magnetic-exchange interaction. It consists of comparing the magnetic properties of two series of isostructural compounds, one composed of Ln–M pairs, the other one of Ln–M′ pairs, M being a paramagnetic and M′ a diamagnetic 3d ion.[35] In our case, these kinds of heterobimetallic compounds cannot be obtained. More recently a quantitative determination of crystal-field parameters for such lanthanide ions[36] has been achieved through the use of the simple overlap model,[37] an extension of purely electrostatic ligand-field theory taking into account some degree of covalence. With the assumption of isotropic coupling, a reasonable fit of the powder susceptibility data was realized in the case of anisotropic lanthanide ions like Dy^{III} and Ho^{III}.[36] One of the most important parameters for determining the nature of the magnetic-exchange interaction with the 4f elements is the crystal field around this 4f element. It has been shown that the number of stark sublevels depends on the Ln^{III} site symmetry.[38]

$[Ln_2(hfac)_5(O_2CPhCl)(L)_3]\cdot 2H_2O$ (Ln = Pr (1) and Gd (2)): The thermal variation of the $\chi_M T$ product for **1** is given in Figure 7 (top). $\chi_M T$ shows a monotonic decrease in the temperature range of 300–2 K taking the values of 3.18–0.17 cm^3 K mol^{-1}, respectively. The first magnetization curve is depicted in Figure S5 in the Supporting Information and shows a linear curve in the field range 0–5 T as usually observed for Pr^{III} complexes. The experimental room-temperature value of $\chi_M T$ is in agreement with the theoretical value of 3.20 cm^3 K mol^{-1} expected for two magnetically isolated Pr^{III} ions.[33] The short metal–metal distance (4.017(1) Å) makes possible the existence of an exchange interaction between the paramagnetic Pr^{III} (J_{Pr-Pr}). Fortunately, Pr^{III} in $Pr(hfac)_3\cdot 3H_2O$ is surrounded by nine oxygen atoms and its coordination sphere can be described as a distorted 4,4,4-tricapped trigonal prism with a D_{3h} symmetry. A similar coordination sphere and symmetry is observed in **1**. Thus, the nature of the exchange interaction J_{Pr-Pr} in **1** can be determined from the comparison of the magnetic properties of **1**

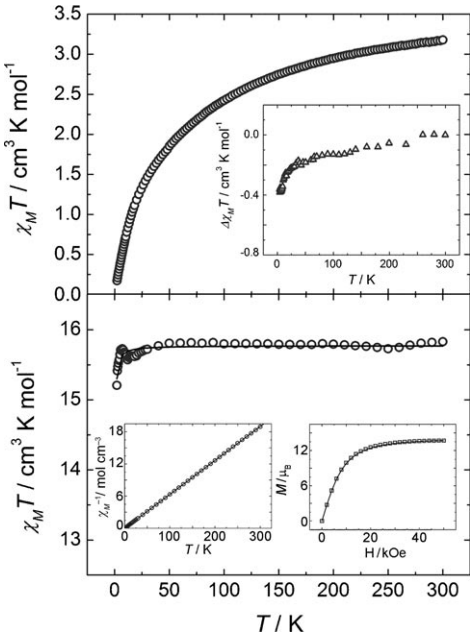

Figure 7. Top: Thermal variation of $\chi_M T$ (gray circles) and $\Delta\chi_M T = \chi_M T_{(1)} - 2\chi_M T_{Pr}$ (gray triangles; in inset) for **1**. Bottom: Thermal variation of $\chi_M T$ (gray circles) with the best fit (solid black line); χ_M^{-1} with Curie–Weiss fit (in inset); and the first magnetization with calculated magnetization for the uncorrelated spin (in inset).

and $Pr(hfac)_3{\cdot}3H_2O$ as defined by the following equation: $\Delta\chi_M T = \chi_M T_{(1)} - 2\chi_M T_{Pr}$ in which $\chi_M T_{(1)}$ and $\chi_M T_{Pr}$ are the $\chi_M T$ product for complex **1** and for the precursor $Pr(hfac)_3{\cdot}3H_2O$, respectively, and $\Delta\chi_M T$ can be considered free of single-ion effects and thus representative of the nature of the exchange interaction between the Pr ^{III} ions (inset of Figure 7). $\Delta\chi_M T(T)$ takes almost constant values from 300 to 40 K and decreases for lower temperatures. The shape of the $\Delta\chi_M T(T)$ curve is in agreement with weak antiferromagnetic exchange interaction ($J_{Pr-Pr} < 0$) between the Pr^{III} ions through the nitroxide group of **L** and 3-chlorobenzoate bridges.

The $\chi_M T$ for **2** is constant (15.83 $cm^3 K mol^{-1}$) in the temperature range 300-40 K (Figure 7). The experimental value of $\chi_M T$ at room temperature is close to that expected for two noninteracting Gd^{III} ($S = {}^7/_2$) ions (15.75 $cm^3 K mol^{-1}$). The case of the Gd^{III} derivative is much easier than that of Pr^{III} due to the absence of anisotropy. The nature of the exchange interaction between the Gd^{III} ions can be determined from the shape of the $\chi_M T(T)$ curve. Thus, **2** has a paramagnetic behavior until 40 K whereas for lower temperatures, weak antiferromagnetic interactions can be observed between the Gd^{III} ions through the **L** and 3-chlorobenzoate bridges. A quantitative determination of the exchange interaction can be performed using Equation (1) derived from the isotropic spin Hamiltonian $H = -JS_{Gd1}S_{Gd2}$, in which J is the exchange interaction constant and S_{Gd1} and S_{Gd2} are the spin operators for the interacting spin centers ($S_{Gd1} = S_{Gd2} = {}^7/_2$).[31]

$$\chi_M T = [(2Ng^2\mu_B{}^2)/k][(140 + 91e^{7x} + 55e^{13x} + 30e^{18x} + 14e^{22x} + 5e^{25x} + e^{27x})/(15 + 13e^{7x} + 11e^{13x} + 9e^{18x} + 7e^{22x} + 5e^{25x} + 3e^{27x} + e^{28x})] \quad (1)$$

In Equation (1), $x = -J/kT$, k = Bolzmann constant, N = Avogadro's number, g = Landé constant, and μ_B = Bohr magneton. The best fit $R = 0.999$ is shown in Figure 7 and J_{Gd-Gd} is found to be equal to (-0.010 ± 0.0008) cm^{-1} with $g_{Gd} = 2.00$. The amplitude of the antiferromagnetic exchange interaction is in agreement with the values of J found in the [{Gd(hfac)$_3$(4-cpyNO)}$_2$] (4-cpyNO = 4-cyanopyridine-*N*-oxide) magnetic systems[31] but smaller than the antiferromagnetic value found in some others compounds.[39] The differences should be due to the change of symmetry around the Gd^{III} centers. The weak antiferromagnetic coupling is confirmed by the Curie–Weiss fit which is performed on the $\chi_M^{-1}(T)$ curve (inset of Figure 7). The data of χ_M^{-1} obey the Curie–Weiss law in the studied range of temperature and the Curie–Weiss fit gives a negative $\theta = -0.01$ K. The experimental first magnetization yields an effective magnetic moment, μ_{eff}, of 13.71μ_B and can be reproduced with a Brillouin function (inset of Figure 7).

$[Tb_2(hfac)_4(O_2CPhCl)_2(L)_2]$ (3): The thermal variation of the $\chi_M T$ product is given in Figure 8. $\chi_M T$ takes a constant value of 23.47 $cm^3 K mol^{-1}$ in the temperature range 300–100 K; this value is close to the expected value for two magnetically isolated Tb^{III} ions (23.64 $cm^3 K mol^{-1}$). The $\chi_M T(T)$ curve shows a monotonic decrease between 100 and 15 K mainly due to the crystal-field effect of the Tb^{III} ions, whereas for cryogenic temperatures it decreases faster perhaps due to some antiferromagnetic exchange interactions in the system. The first magnetization curve is depicted in Figure S6 in the Supporting Information. It shows a fast increase for low magnetic fields and a smooth linear increase in the field range 1.5–5 T without reaching the saturated effective moment. The method used for the determination of the exchange interaction in **1** can be adapted in the case of **3**. In fact, the structural analysis has revealed a dodecahedral coordination sphere for the Tb^{III} centers in **3** as ob-

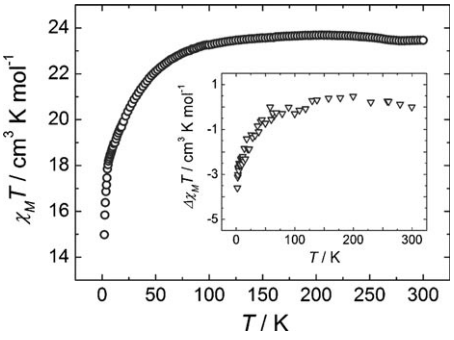

Figure 8. Thermal variation of $\chi_M T$ for **3** (gray circles). Inset: thermal variation of $\Delta\chi_M T = \chi_M T_{(3)} - 2\chi_M T_{Tb}$ (gray triangles).

served in the crystal structure of the precursors Ln-(hfac)$_3$·2H$_2$O (Ln = Gd–Lu).[40] The expression of the magnetic coupling constant between the Tb^{III} ions through the bridging 3-chlorobenzoate anions can be written as $\Delta\chi_M T = \chi_M T_{(3)} - 2\chi_M T_{Tb}$ in which the parameters are defined as previously for terbium instead of praseodymium. The $\Delta\chi_M T(T)$ is presented in the inset of Figure 8. The value of $\Delta\chi_M T(T)$ remains almost equal to 0 down to 50 K and decreases for lower temperatures. The shape and sign of the $\Delta\chi_M T(T)$ curve attests that a weak antiferromagnetic exchange interaction ($J_{Tb-Tb} < 0$) takes place between the Tb^{III} ions through the 3-chlorobenzoate bridges.

[Yb(hfac)$_3$(L)$_2$] (5): The $\chi_M T(T)$ curve for **5** is depicted in Figure 9. It takes a room temperature value of 2.49 cm^3 K mol^{-1} and shows a monotonic decrease until 2 K. The value at 300 K is close to the expected value for one non-interacting magnetic Yb^{III} ion (2.57 cm^3 K mol^{-1}), whereas the decrease of the $\chi_M T(T)$ curve is only attributed to the crystal field of the metal ion. In the inset, the first magnetization for **5** is shown. It reveals a classic behavior for such a lanthanide ion.

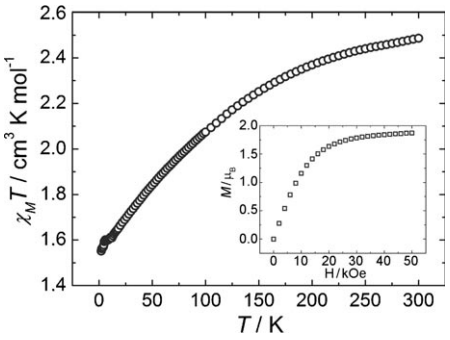

Figure 9. Thermal variation of $\chi_M T$ and the first magnetization for **5** (inset).

UV-visible absorption spectroscopy: The UV-visible absorption spectra have been recorded in the solid state at room temperature. The maxima for absorption bands have been determined with Gaussian deconvolution of the experimental data. The UV-visible absorption spectroscopy of donor **L** has been studied in our previous work.[20] The absorption spectrum of **L** is depicted in Figure 10 for comparison with spectra of complexes **1**–**5**.

*Complexes **1**–**3***: The UV-visible absorption spectra are depicted in Figure 10 (for **1** and **3**) and Figure S7 in the Supporting Information (for **2**). All spectra are composed of two multiple-absorption bands and are mainly composed of the absorption bands of the free donor **L** (black deconvolutions) and two additional transitions (dashed deconvolutions; Figure 10). The lowest energy absorption band is deconvoluted in two absorption bands centered at mean values of 18000 and 21400 cm^{-1} (Table 6). These absorption bands are usually attributed to monoelectronic donor–acceptor charge transfer (DACT) transitions from the highest occupied molecular orbital centered on the TTF fragment to the lowest unoccupied molecular orbital centered on the acceptor.[19,41] In the case of free donor, such DACTs correspond to HOMO→LUMO transitions that can be written HOMO−(m)→LUMO+(n) for the complexes (see the DFT calculations on **4**). For free donors, the presence of two DACTs has been explained by the existence of intermolecular DACTs between the packed donors in the solid state.[20] To verify this explanation in the case of donor **L**, the solid-state UV-visible spectrum was compared with those in solution (Figure S8 in the Supporting Information). In weakly dissociating solvent (CH_2Cl_2), two DACTs are again observed due to the probable presence of stacked donors in such a solvent, whereas in strongly dissociating solvent (di-

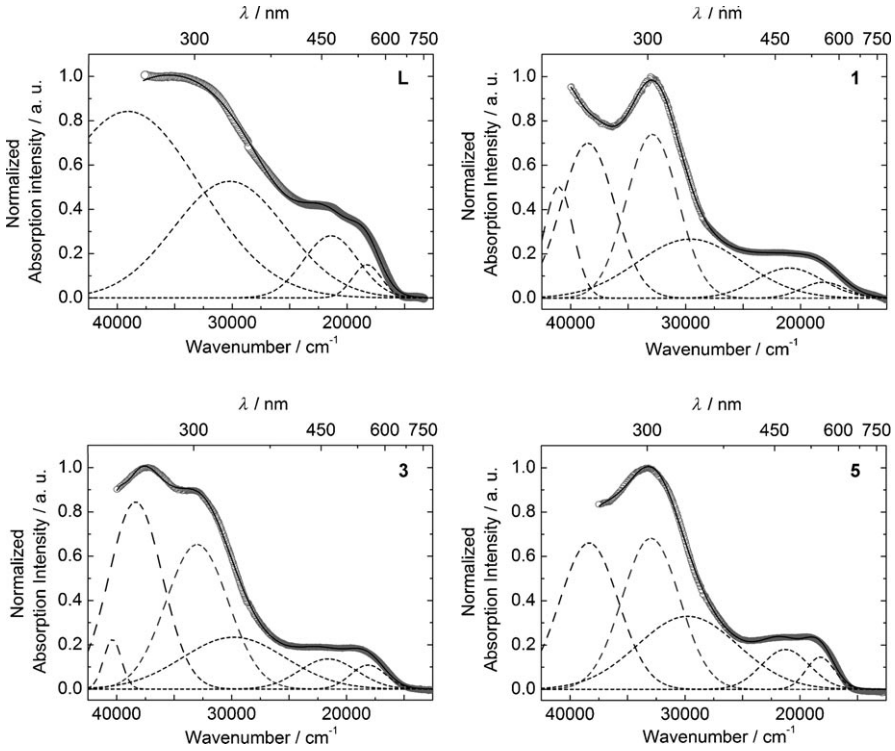

Figure 10. Experimental solid-state (KBr pellets) UV/Vis absorption spectra (open circles), respective Gaussian deconvolutions (dashed lines), and best fit (solid black line): $R = 0.9994$ (for **L**), $R = 0.9999$ (for **1**), $R = 0.9997$ (for **3**), and $R = 0.9992$ (for **5**).

Table 6. Experimental UV-visible absorption spectroscopic data[a] ($\tilde{\nu}$ in cm^{-1}) for complexes **1**–**5**.

1	2	3	4	5
41000	40700	40400	–	–
38500	38400	38400	38600	38300
32900	33000	33000	32800	33000
29600	29800	29800	29500	29800
21000	21700	21600	21000	21300
18000	18000	18100	18200	18200

[a] The values correspond to the maxima of the absorption bands, which are determined by Gaussian deconvolutions.

methylformamide), only one DACT band is observed. It is reasonable to think, that this phenomenon is similar for the complexes. Unfortunately, it is not possible to perform similar solution measurements due to the partial or full destruction of the complexes in strong dissociating solvent. Four absorption bands are deconvoluted up to 27500 cm^{-1}. The two centered at about 29700 and 38400 cm^{-1} are attributed to intramolecular $\pi\rightarrow\pi^*$ transitions of the pyridine-*N*-oxide acceptor. The two additional absorption bands, relative to the spectrum of free donor **L**, come from intramolecular $\pi\rightarrow\pi^*$ transitions of the $hfac^-$ anions (about 33000 cm^{-1}) and from the 3-chlorobenzoate anions (about 40700 cm^{-1}). To carry on with the qualitative analysis, a comparison between the absorption spectra of **L** and the complexes can be realized. In the complexes, the intramolecular $\pi\rightarrow\pi^*$ transitions of the pyridine-*N*-oxide acceptor and the DACTs are redshifted by about 600 and 200 cm^{-1}, respectively. These bathochromic shifts are due to the Lewis acidity of Ln^{III}, which leads to a decrease of the electron density on the pyridine-*N*-oxide moiety that causes 1) the energy stabilization of the π^* orbital of the substituent, 2) the energy destabilization of the π orbital of the substituent, and thus the energy decrease of both intramolecular $\pi\rightarrow\pi^*$ and DACTs transitions. It is worth noting that probably like for **4** (see the theoretical calculations), the orbitals that are centered on the acceptor are affected by the complexation of the lanthanide, whereas those centered on the TTF core remain almost unchanged. This is supported by the unchanged electrochemical properties between the free donor **L** and the complexes, and can explain the most important shift for the $\pi\rightarrow\pi^*$ transitions with respect to DACTs. Similar redshifts of the absorption bands upon complexation have already been observed in our previous work on the mononuclear Gd^{III} complex with the TTF-amido-2-pyrimidine-1-oxide ligand.[19]

No significant change is expected between 4f elements with similar ionic radii. In addition, it is well known that, within an isostructural series, all complexes present very similar absorption spectra regardless of the nature of the lanthanide ion.[42] This similar ionochromic effect is verified for complexes **1**–**3** containing Pr, Gd, and Tb, respectively, and **4** and **5** containing Y and Yb, respectively, that exhibit very similar solid-state absorption spectra (Table 6). Therefore it should be correct to extrapolate the theoretical results of **4** to **5** to interpret their optical properties. In consequence, it appears that the irradiation of **5** with energy close to that of the maximum of the DACT, is a judicious choice to study the emission properties of **5**.

*Complexes **4** and **5***: The UV-visible absorption spectra are depicted in Figure 10 (for **5**), Figure S7 in the Supporting Information (for **4**), and Table 6. The UV spectra of the mononuclear complexes are similar to those for the dinuclear compounds. The principal difference is the disappearance of the absorption band localized at 40700 cm^{-1} due to the absence of 3-chlorobenzoate in the crystal structures of mononuclear complexes **4** and **5**.

Time-dependent (TD) DFT calculations on complex 4: To get more insight into the absorption properties, TD-DFT calculations were performed on the Y^{III} complex, a diamagnetic model without f–f excited states (see the computational details in the Experimental Section). Molecular orbital diagrams (Figure 11) and calculated UV-visible spectra (Figure 12) of **4** have been determined and compared with that of free ligand **L** previously published.[20] The simulation of the shape of the UV-visible absorption spectra by TD-DFT calculations is in good agreement with the experimental data. A hypsochromic shift of the absorption maxima is observed at high energy (up to 25000 cm^{-1}) between calculated (gas phase) and experimental data recorded in the solid state. On the contrary, the solution UV-visible spec-

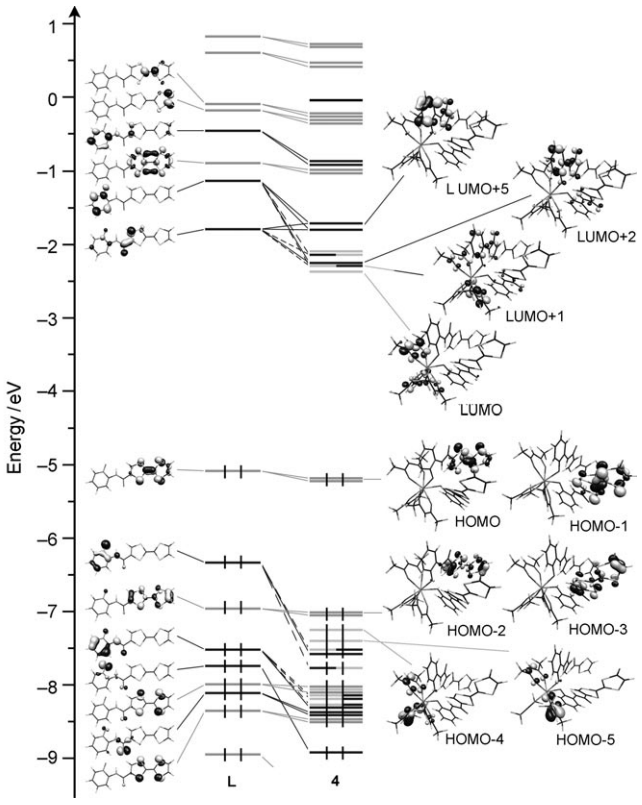

Figure 11. Molecular orbital diagram of **L** and **4**. Energy level of the centered $hfac^-$, TTF (D), and PyNO (A) orbitals are represented in light gray, gray, and black, respectively.

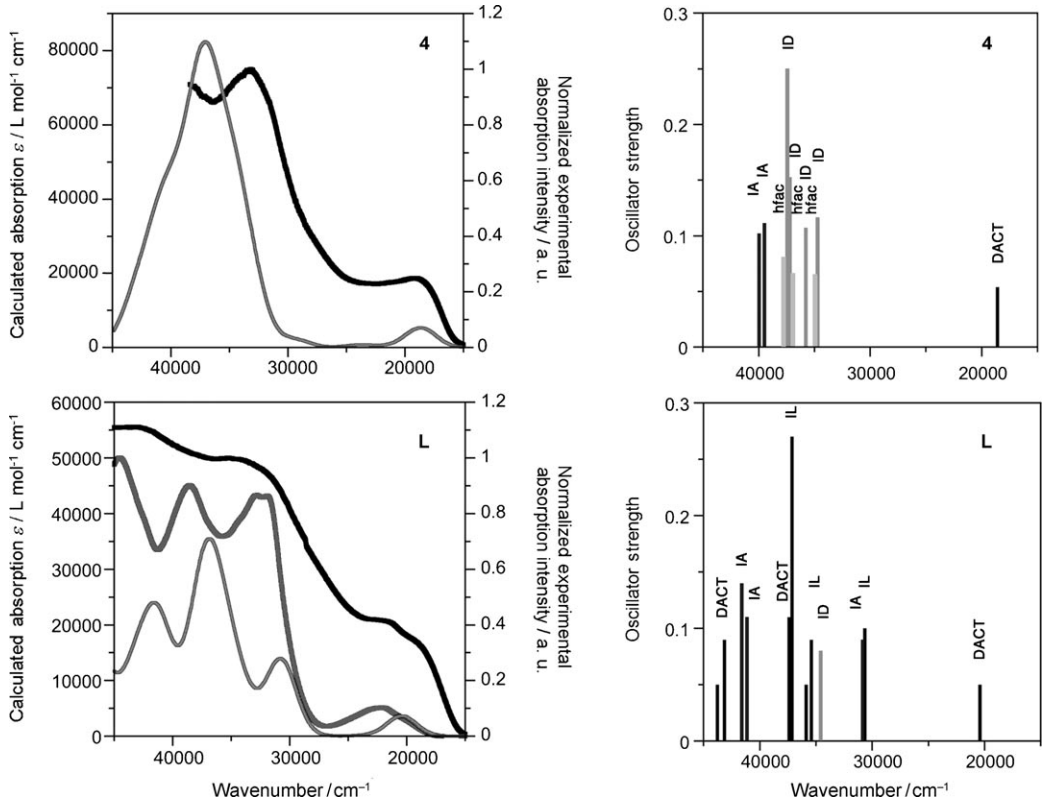

Figure 12. Left: theoretical and experimental absorption spectra of compounds **4** and **L**. Solid-state and solution (CH_3CN) measurements correspond respectively to black and dark gray lines, whereas the light gray lines correspond to calculated spectra. Right: most pertinent low-lying electronic transitions and assignment of compounds **4** and **L**.

trum of **L** is very well reproduced without a shift of the absorption maxima (bottom of Figure 12).

For complex **4**, the major part of the experimental lowest-energy deconvolution centered at the mean value of 19600 cm^{-1} is identified as intramolecular charge transfers HOMO→LUMO+1/LUMO+2 (Table 7). The HOMO is centered on the TTF core whereas the LUMO+1 and LUMO+2 are centered on the amidopyridine-*N*-oxide acceptor (called A) (Figure 11). The energy of this CT is calculated at 18611 cm^{-1}.

The experimental deconvolution centered at 29500 cm^{-1} is attributed to several intra-TTF moiety transitions. The most intense excitations are calculated at the following energies: 34739, 35802, 37274, and 37475 cm^{-1}. The TD-DFT calculations show that these excitations are attributed to the following transitions: HOMO−3→LUMO+7, HOMO−1→LUMO+13/LUMO+18, and HOMO→LUMO+14/LUMO+16/LUMO+17/LUMO+19 (Table 7). The electronic density in all theses orbitals are localized on the TTF core (Figure 11).

The third experimental deconvolution centered at 32800 cm^{-1} is attributed to π→π* intra-hfac$^-$ (Ihfac$^-$) excitations that are mainly composed of the three HOMO−4→

Table 7. TD-DFT-calculated excitation energies and main composition of low-lying electronic transitions of **4** associated with an oscillator strength of $f>0.07$ except for the lowest excitation. In addition, the visible-range charge transfer and the pure intramolecular transition-centered hfac$^-$ ligands are reported.

Energy [cm^{-1}] exptl	theor	Oscillation	Type[a]	Assignment[b]	Transition[c]
19600	18611	0.05	DACT	$\pi^{nb}_{TTF}\rightarrow\pi^{*}_{pyNO}$	H→L+1/L+2 (72%)
29500	34739	0.12	ID	$\pi^{nb}_{TTF}\rightarrow\pi^{*}_{TTF}/\sigma^{*}_{TTF}$	H−3→L+7 (12%) H−1→L+13/L+18 (41%)
	35802	0.11	ID	$\pi^{nb}_{TTF}\rightarrow\pi^{*}_{TTF}/\sigma^{*}_{TTF}$	H→L+14/L+16/L+17 (73%)
	37274	0.15	ID	$\pi^{nb}_{TTF}\rightarrow\sigma^{*}_{TTF}$	H−1→L+18 (13%) H→L+19 (13%)
	37475	0.25	ID	$\pi^{nb}_{TTF}\rightarrow\pi^{*}_{TTF}/\sigma^{*}_{TTF}$	H−1→L+13/L+18 (39%) H→L+19 (13%)
32800	34900	0.07	Ihfac$^-$	$\pi^{nb}_{hfac-}\rightarrow\pi^{*}_{hfac-}$	H−4→L+2 (36%)
	36959	0.07	Ihfac$^-$	$\pi^{nb}_{hfac-}\rightarrow\pi^{*}_{hfac-}$	H−5→L+4 (36%)
	37826	0.08	Ihfac$^-$	$\pi^{nb}_{hfac-}\rightarrow\pi^{*}_{hfac-}$	H−5→L+3 (35%)
38600	39484	0.11	IA+Ihfac$^-$	$\pi^{nb}_{pyNO}/\pi^{nb}_{hfac-}\rightarrow\pi^{*}_{pyNO}/\pi^{*}_{hfac-}$	H−8→L+1 (19%)
	40002	0.10	IA+Ihfac$^-$	$\pi^{nb}_{pyNO}/\pi^{nb}_{hfac-}\rightarrow\pi^{*}_{pyNO}/\pi^{*}_{hfac-}$	H−8→L+2/L+4 (26%) H−4→L+5 (10%)

[a] ID, IA, and Ihfac$^-$ represent the intramolecular TTF (donor), pyNO (acceptor), and hfac$^-$ transitions and therefore DACT stands for donor-to-acceptor charge transfer. [b] nb represents nonbonding orbitals. [c] H and L represent the HOMO and LUMO, respectively.

LUMO+2 (calculated at 34900 cm^{-1}) and HOMO−5→LUMO+3/LUMO+4 (calculated at 36959 and 37826 cm^{-1}, respectively) transitions (Table 7).

Finally, the highest-energy experimental deconvolution (38600 cm^{-1}) is identified as π→π* intra-amidopyridine-*N*-oxide acceptor (IA) excitation with a participation of the π→π* intra-hfac$^-$ ones. These excitations are attributed to the HOMO−8→LUMO+1 and HOMO−4→LUMO+5 transitions with a calculated absorption maximum at 39743 cm^{-1}.

The molecular orbital diagrams of **L** and **4** highlight the coordination effect of the Y^{III} ions on the energy level of the orbitals (Figure 11). So the coordination of this ion leads to an energy stabilization of the centered acceptor orbitals (blue levels) as expected because the coordination takes place through the N−O group of the 2-pyridine-*N*-oxide moiety; whereas the TTF-centered orbitals (dark gray levels) are only weakly stabilized due to the long pathway between the TTF core and the N−O group. Nevertheless, a significant electronic effect of the Y^{III} coordination is observed through the amido bridge. The coordination of the Y^{III} ion also induces a better localization of the orbitals on the TTF core and acceptor moiety. Thus the π→π* intraligand (IL) excitations for free ligand **L** disappear to give π→π* intradonor (ID) and/or intraacceptor (IA) excitations in complex **4** (right part of the Figure 12). The most important consequence of the stabilization of the acceptor-centered orbitals is the redshift of the CT in **4** relative to **L** (about 2260 cm^{-1}). Redshift of the IA excitations is also observed and calculated (about 3500 cm^{-1}). The TD-DFT theoretical calculations are in agreement with the experimental observations. Ligand **L** has been coordinated to $M(hfac)_2$ metallic precursors (M^{II}=Cu, Mn, and Zn) in our previous work.[20] The coordination of various divalent metal ions with **L** has permitted the demonstration that the coordination effect is essentially an electrostatic effect. In the case of M^{II} ions, the redshift of the DACT has been calculated to be 2900 cm^{-1}, which is slightly greater than the one observed for the coordination of Y^{III}. On one side, it is expected that the electrostatic effect increases with trivalent ion relative to a divalent one. On the other side, the longer Y−O bond lengths (2.335(3) Å) compared with those of M−O (1.998(2) Å) lead to the decrease of this effect. In conclusion, oxidation degrees and bond lengths compensate each other.

Luminescence properties of L and $[Ln(hfac)_3(L)_2]$ (Ln=Y (4) and Yb (5)): Upon excitation in the lower energy DACT transition (λ_{ex}=510 nm, 19600 cm^{-1}), both free ligand **L** and yttrium complex **4** exhibit a broad fluorescence band centered at 715 and 737 nm (13986 and 13568 cm^{-1}), respectively.

The bathochromic shift observed in the absorption spectra upon complexation is amplified in the emission spectra thereby confirming the CT character of these transitions. TTF-fused phenazine ligands featuring a strong CT transition are known to exhibit an emission band in a similar wavelength range and to present an analogous bathochromic shift upon complexation with transition-metal ions.[41,43] In the case of ytterbium complex **5**, excitation in the same CT transition (λ_{ex}=510 nm, 19600 cm^{-1}) induces the line-shape emissions in the NIR spectral range assigned to the $^2F_{5/2}\rightarrow{}^2F_{7/2}$ (980 nm) transition centered on the ytterbium ion. In addition, the residual CT emission is observed around 760 nm (13157 cm^{-1}) (Figure 13). It is worth noting that this

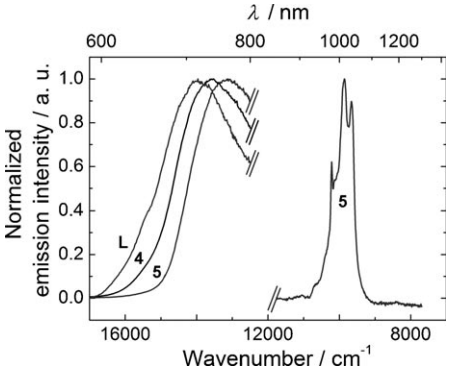

Figure 13. Emission spectra of **L**, **4**, and **5** in the near-IR region for λ_{ex}= 19600 cm^{-1} at room temperature (293 K) in the solid state.

residual CT emission is slightly redshifted with respect to that of the yttrium complex. A similar bathochromic shift in the ligand CT emission along the 4f element row has already been described and is generally explained by the enhanced sensitivity of luminescence transitions to the central ion Lewis acidity compared with that of the absorption. In the present case, the Yb^{III} ion is smaller than Y^{III} and then presents a more Lewis acid character and consequently a larger redshift in the CT emission.[13d] It is worth noting that the presence of these low-energy CT transitions allows the sensitization of Yb^{III} with long wavelength up to 500 nm localized in the visible part of the spectra. The energy of the donor excited state can be estimated from the zero-phonon transition wavelength $\lambda_{0\text{-}0}$ estimated to be 635 nm (15750 cm^{-1}) from the intersection of the absorption and emission spectra. This result is in the range of the longest wavelengths reported for the Yb sensitization using antenna featuring xanthene (fluroescein, eosin, erythrosine, or rhodamine 6G, 500–550 nm),[44] Bodipy (530 nm),[45] or push–pull (550 nm)[46] chromophores.

In the particular case of Yb^{III}, the sensitization process remains a matter of debate due to the presence of a single excited state responsible for the absorption and emission. The sensitization can proceed either through energy transfer from the triplet or the singlet excited state of a chromophore antenna or through a stepwise photoinduced electron transfer in the case of electroactive ligands. This latter process restricted to Ln^{III} ions that can be reduced at a rather modest potential was initially proposed by Horrocks[47] and extensively studied by Faulkner and Ward.[18,48] It involves the transient formation of an oxidized donor/Yb^{II} species that will generate the emissive Yb^{III} excited state after back-

electron transfer. Due to the presence of an electroactive TTF-containing ligand[18] in complex **5**, this sensitization process must be considered. According to the above-mentioned studies,[18,47,48] it is possible to estimate the feasibility of the photoinduced electron transfer (ΔG_{ET}) using the extended Raehm–Weller[49] Equation (2):

$$\Delta G_{ET} \geq e_0(E_{ox}-E_{red})-E_s-w \quad (2)$$

in which e_0 represents the elementary electron charge, E_{ox}, the oxidation potential of the electrodonating ligand, E_{red}, the reduction potential of the acceptor, and E_s, the excited-state energy. In addition, w represents the stabilization energy between the different components of the ion pair (0.15 eV for a closely associated ion pair). In the present case, the oxidation potential of the TTF moieties in **5** is estimated to be 0.512 V versus the saturated calomel electrode (SCE) from cyclic voltammetry. On the other hand, the reduction potential of the couple $[Yb^{III}(hfac)_3(H_2O)_2]/[Yb^{II}(hfac)_3(H_2O)_2]$ is found to be −1.65 V versus SCE. The energy of the excited state corresponds to the zero-phonon transition, $E_s = E_{0\text{-}0} = 1.95$ eV; Equation (2) becomes $\Delta G_{ET} \geq 1\times(0.512+1.65)-1.95-0.15$ hence $\Delta G_{ET} \geq 0.112$ eV. Since ΔG_{ET} is a positive value, the electron-transfer process is not thermodynamically favored suggesting that the sensitization occurs through an antenna effect.

This antenna-mediated sensitization process generally involves a resonant energy-transfer process (Forster or Dexter mechanism) and therefore requires an overlap between the emission of the donating state and the absorption of the central metal ion.[8] As a general rule, the energy level of the donating state must lie at about 2–3000 cm^{-1} above that of the accepting state to optimize the energy transfer and avoid the thermally activated back-energy transfer. In the case of ytterbium the $^2F_{7/2}\rightarrow{}^2F_{5/2}$ absorption is located at 10240 cm^{-1} so a good antenna should present a donating state around 12–13000 cm^{-1}. Since the triplet state associated to the $hfac^-$ ligand lies around 21370 cm^{-1} (in the analogous Gd complex),[31] the lowest excited state in **5** is the charge-transfer state. It is worth noting that the CT excited state is known to present significant relaxation in their excited state, so the energy of the donating state is better described by the CT emission band by taking into account its broadness.[13d] In the present case (Figure 13), the emission band starts with the zero-phonon transition (15750 cm^{-1}), presents a maximum around 13160 cm^{-1}, and its red tail can be estimated as 11360 cm^{-1} using a rough deconvolution into the Gaussian function. (The detection setup is blind in the 800–950 nm region). The energy of the donating CT, comprising the 15750–11360 cm^{-1} energy range, is located at the optimal position to efficiently sensitize the Yb^{III} luminescence. Finally, the most probable sensitization process in **5** (Figure 14) involves a direct sensitization through the singlet CT state.[13d,44–46]

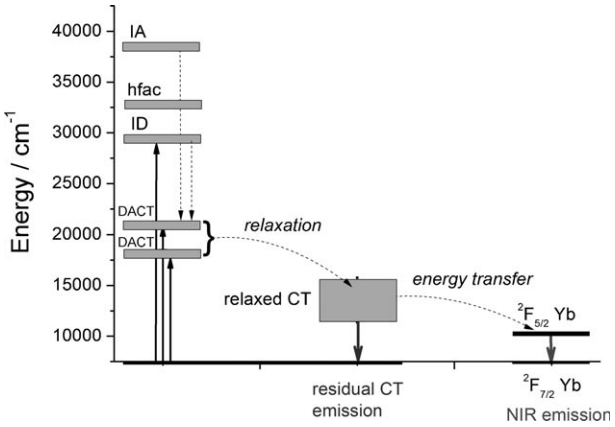

Figure 14. Probable sensitization process in **5**.

Conclusion

In this work, five lanthanide-based coordination complexes involving the redox-active tetrathiafulvalene-amido-2-pyridine-*N*-oxide ligand (**L**) have been synthesized and their crystal structures have been resolved by X-ray diffraction. Three crystal-structural families have been identified and they are obtained roughly depending of the ionic radius of the trivalent lanthanides.

After canceling the crystal-field contribution of the lanthanides by an extended empirical method, antiferromagnetic exchange interactions have been identified between the lanthanide centers through the nitroxide group of **L** and 3-benzoic acid bridges.

All the complexes have been investigated by solid-state UV-visible absorption spectroscopy. Gaussian deconvolutions of the experimental curves were performed to fit the data. The molecular-orbital diagram for the diamagnetic Y^{III} derivative has been elaborated and TD-DFT calculations have permitted the reproduction of the absorption spectra. The low-energy transitions are identified as monoelectronic HOMO→LUMO+1/LUOM+2 charge transfers from the TTF core to the amido-2-Py-*N*-oxide acceptor. The intermediate-energy region is composed of intra-TTF (29500 cm^{-1}) and intra-$hfac^-$ (32800 cm^{-1}) π–π* transitions, whereas the high-energy region is composed of intra-acceptor (38600 cm^{-1}) π–π* excitations. The coordination effects of the $Ln(hfac)_3$ moiety are highlighted by a redshift of the absorption transitions relative to free **L**. Irradiation of the HOMO→LUMO+1/LUMO+2 charge-transfer transitions (19600 cm^{-1}) of both $[Ln(hfac)_3(\mathbf{L})_2]$ compounds (Ln^{III} = Y (**4**) and Yb (**5**)) induces a broad fluorescence band centered at 13568 and 13157 cm^{-1}, respectively. In the case of **5**, the excitation induces line-shape emissions in the near-infrared spectral range assigned to the $^2F_{7/2}\rightarrow{}^2F_{5/2}$ (9860 cm^{-1}) transition centered on the ytterbium ion. The positive value for the photoinduced electron-transfer parameter ($\Delta G_{ET} \geq 0.112$ eV) suggests that the antenna-effect sensitization process is favored and proceeds through energy transfer from the singlet CT state of the **L** chromophore. It is worth

noting that the energy of the charge-transfer donation is estimated to be 15750 cm^{-1}, which is in the range of the longest wavelengths reported for Yb^{III} sensitization. The energy is localized in the optimal energy range leading to the fact that **L** is an efficient charge-transfer antenna ligand for the sensitization of Yb^{III} luminescence.

Electrochemical oxidations are under investigation to obtain oxidized coordination complexes and to study the influence of the oxidation state of **L** on infrared emissions. In addition, synthetic efforts are in progress in the group to elaborate new infrared luminescent lanthanide-based complexes that should be stable in solution and suitable for grafting on a surface.

Experimental Section

General procedures and materials: All solvents were dried using standard procedures. The precursors $Ln(hfac)_3{\cdot}xH_2O$ ($hfac^- = 1,1,1,5,5,5$-hexafluoroacetylacetonate anion; $Ln^{III} = Pr$, $x = 3$; and for $Ln^{III} = Gd$, Tb, Y and Yb, $x = 2$)[50] and 2-pyridyl-*N*-oxide-carbomoyltetrathiafulvalene (**L**)[20] were synthesized following previously reported methods. All other reagents were purchased from Aldrich Co. Ltd and were used without further purification.

Crystallography: Single crystals were mounted on a Nonius four-circle diffractometer equipped with a CCD camera and a graphite-monochromated $Mo_{K\alpha}$ radiation source ($\lambda = 0.71073$ Å), from the Centre de Diffractométrie (CDFIX), Université de Rennes 1, France. Data were collected at 293 K. Structures were solved with a direct method using the SIR-97 program and refined with a full-matrix least-squares method on F^2 using the SHELXL-97 program.[51] Crystallographic data are summarized in Table 1. CCDC-776876 (**1**), -776877 (**2**), -776878 (**3**), -776879 (**4**), and 776880 (**5**) contain the supplementary crystallographic data for this paper. These data can be obtained free of charge from The Cambridge Crystallographic Data Centre via www.ccdc.cam.ac.uk/data_request/cif.

Physical measurements: Cyclic voltammetry was carried out on solutions of the compounds in acetonitrile containing 0.1 M $N(C_4H_9)_4PF_6$ as supporting electrolyte. Voltammograms were recorded at 100 $mV\,s^{-1}$ at a platinum disk electrode. The potentials were measured versus a saturated calomel electrode (SCE; Table 5). Optical spectra were measured using the KBr disk method on Perkin–Elmer 1600 Series FTIR (resolution 4 cm^{-1}) for infrared (IR) spectroscopy. Absorption spectra were recorded using the KBr disk method on a Varian Cary 5000 UV-visible-NIR spectrometer equipped with a diffuse reflectance accessory. The luminescence spectra were measured using a Horiba-Jobin Yvon Fluorolog-3 spectrofluorimeter, equipped with a three-slit double-grating excitation and emission monochromator with dispersions of 2.1 $nm\,mm^{-1}$ (1200 $grooves\,mm^{-1}$). The steady-state luminescence was excited by unpolarized light from a 450 W xenon continuous wave (CW) lamp and detected at an angle of 90° for diluted solution measurements or at 22.5° for solid-state measurements (front face detection) by a red-sensitive Hamamatsu R928 photomultiplier tube. Spectra were reference-corrected for both the excitation-source light-intensity variation (lamp and grating) and the emission spectral response (detector and grating). Uncorrected near-IR spectra were recorded at an angle of 45° using a liquid-nitrogen-cooled, solid indium/gallium/arsenic detector (850–1600 nm). The direct current (dc) magnetic susceptibility measurements were performed on solid polycrystalline samples with a Quantum Design MPMS-XL SQUID magnetometer between 2 and 300 K in an applied magnetic field of 0.2 T for temperatures of 2–20 K and 1 T for temperatures of 20–300 K. The experimental data have been corrected from the diamagnetism of the sample holder, and the intrinsic diamagnetism of the materials was evaluated with Pascal's tables.

Computational details: The UV-visible absorption spectra of ligand **L** and complex **4** have been calculated. At first, a full geometry optimization of **4** was carried out using DFT methods from the solid-state geometry. All calculations were performed with the hybrid functional adaptation of PBE[52] (usually referred to as PBE0) as implemented in the Gaussian 03 program.[53] Previous tests on **L** with the GGA functional BP86[54] led to very similar results.[20] To manage the calculations on the whole complex **4**, we used a double-ζ-quality basis set proposed by Weigend et al. with polarization functions for all atoms.[55] The difference with a triple-ζ-quality basis set was previously probed on **L** and was found to be negligible.[20] Then, the first 150 low-lying monoelectronic excitations (up to 53000 cm^{-1}) were computed using a time-dependent density functional theory (TD-DFT) procedure with the same program, functional, and basis set as the first step.

Synthesis of $[Pr_2(hfac)_5(O_2CPhCl)(L)_3]{\cdot}2H_2O$ (1): $Pr(hfac)_3{\cdot}3H_2O$ (24.6 mg, 0.03 mmol) was dissolved in CH_2Cl_2 (5 mL); then a solution of ligand **L** (25.4 mg, 0.075 mmol) and 3-chlorobenzoic acid (4.7 mg, 0.03 mmol) in CH_2Cl_2 (5 mL) was slowly added. After 20 min of stirring, the dark red solution was put in a closed flask and *n*-hexane solvent was slowly diffused in the dark. After two weeks, dark red single crystals of **1** were obtained. Yield: 11.0 mg (29%); IR: $\tilde{\nu} = 3451$, 3142, 2928, 2854, 1698, 1678, 1649, 1530, 1512, 1436, 1340, 1256, 1205, 1146, 800, 764, 659, 585 cm^{-1}.

Synthesis of $[Gd_2(hfac)_5(O_2CPhCl)(L)_3]{\cdot}2H_2O$ (2): This complex was synthesized by a similar procedure to that used for **1** starting from $Gd(hfac)_3{\cdot}2H_2O$ (24.4 mg, 0.03 mmol). After two weeks of slow diffusion of *n*-hexane in the mother liquor in the dark, dark red single crystals of **2** were obtained. Yield: 10.2 mg (27%); IR: $\tilde{\nu} = 3450$, 3140, 2929, 2854, 1698, 1673, 1654, 1582, 1512, 1435, 1315, 1254, 1205, 1143, 797, 763, 659, 584 cm^{-1}.

Synthesis of $[Tb_2(hfac)_4(O_2CPhCl)_2(L)_2]$ (3): This complex was synthesized by a similar procedure to that used for **1** starting from $Tb(hfac)_3{\cdot}2H_2O$ (24.4 mg, 0.03 mmol). After four weeks of slow diffusion of *n*-hexane in the mother liquor in the dark, dark red single crystals of **3** were obtained. Yield: 13.0 mg (40%); IR: $\tilde{\nu} = 3433$, 3138, 2928, 2851, 1694, 1668, 1650, 1586, 1558, 1524, 1513, 1434, 1255, 1211, 1144, 798, 742, 661, 586 cm^{-1}.

Synthesis of $[Y(hfac)_3(L)_2]$ (4): This complex was synthesized by a similar procedure to that used for **1** starting from $Y(hfac)_3{\cdot}2H_2O$ (22.4 mg, 0.03 mmol). After one week of slow diffusion of *n*-hexane in the mother liquor in the dark, dark red blocks single crystals of **4** were obtained. Yield: 17.4 mg (42%); IR: $\tilde{\nu} = 3342$, 3130, 2935, 2848, 1670, 1650, 1582, 1557, 1534, 1517, 1437, 1257, 1212, 1144, 800, 766, 660, 642, 586 cm^{-1}.

Synthesis of $[Yb(hfac)_3(L)_2]$ (5): This complex was synthesized by a similar procedure to that used for **4** starting from $Yb(hfac)_3{\cdot}2H_2O$ (25.4 mg, 0.03 mmol). After one week of slow diffusion of *n*-hexane in the mother liquor in the dark, dark red blocks single crystals of **5** were obtained. Yield: 32.0 mg (72%); IR: $\tilde{\nu} = 3339$, 3134, 2938, 2849, 1670, 1651, 1581, 1557, 1536, 1518, 1437, 1258, 1212, 1143, 799, 766, 661, 643, 585 cm^{-1}.

Acknowledgements

This work was supported by the CNRS, MAGMANet European excellence network, Université de Rennes 1 and la Région Bretagne.

[1] a) H. Kobayashi, H. Tomita, T. Naito, A. Kobayashi, F. Sakai, T. Watanabe, P. Cassoux, *J. Am. Chem. Soc.* **1996**, *118*, 368; b) H. Kobayashi, A. Kobayashi, P. Cassoux, *Chem. Soc. Rev.* **2000**, *29*, 325; c) A. Kobayashi, E. Fijiwara, H. Kobayashi, *Chem. Rev.* **2004**, *104*, 5243, and references therein; d) T. Enoki, A. Miyasaki, *Chem. Rev.* **2004**, *104*, 5449; e) M. Kurmoo, A. W. Graham, P. Day, S. J. Coles, M. B. Hurtsthouse, J. M. Caufield, J. Singleton, L. Ducasse, P. Guionneau, *J. Am. Chem. Soc.* **1995**, *117*, 12209; f) E. Coronado, P. Day, *Chem. Rev.* **2004**, *104*, 5419 and the references therein; g) L. Ouahab, T. Enoki, *Eur. J. Inorg. Chem.* **2004**, 933; h) D. Lorcy, N. Bellec, M. Fourmigué, N. Avarvari, *Coord. Chem. Rev.* **2009**, *253*, 1398, and ref-

erences therein; i) M. Fourmigué, L. Ouahab, *Conducting and Magnetic Organometallic Molecular Materials*, Springer, Heidelberg, **2009**.

[2] a) E. Ojima, H. Fujiwara, K. Kato, H. Kobayashi, H. Tanaka, A. Kobayashi, M. Tokumoto, P. Cassoux, *J. Am. Chem. Soc.* **1999**, *121*, 5581; b) H. Fujiwara, E. Ojima, Y. Nakazawa, B. Narymbetov, K. Kato, H. Kobayashi, A. Kobayashi, M. Tokumoto, P. Cassoux, *J. Am. Chem. Soc.* **2001**, *123*, 306; c) T. Otsuka, A. Kobayashi, Y. Miyamoto, J. Kiuchi, N. Wada, E. Ojima, F. Fujiwara, H. Kobayashi, *Chem. Lett.* **2000**, 732; d) T. Otsuka, A. Kobayashi, Y. Miyamoto, J. Kiuchi, S. Nakamura, N. Wada, E. Fujiwara, H. Fujiwara, H. Kobayashi, *J. Solid State Chem.* **2001**, *159*, 407; e) H. Kobayashi, A. Sato, E. Arai, H. Akutsu, A. Kobayashi, P. Cassoux, *J. Am. Chem. Soc.* **1997**, *119*, 12392; f) A. Sato, E. Ojima, H. Akutsu, Y. Nakazawa, H. Kobayashi, H. Tanaka, A. Kobayashi, P. Cassoux, *Chem. Lett.* **1998**, 673; g) H. Tanaka, H. Kobayashi, A. Kobayashi, P. Cassoux, *Adv. Mater.* **2000**, *12*, 1685; h) S. Uji, H. Shinagawa, T. Terashima, C. Terakura, T. Yakabe, Y. Terai, M. Tokumoto, A. Kobayashi, H. Tanaka, H. Kobayashi, *Nature* **2001**, *410*, 908.

[3] a) S. Bouguessa, A. K. Gouasmia, S. Golhen, L. Ouahab, J.-M. Fabre, *Tetrahedron Lett.* **2003**, *44*, 9275; b) S.-X. Liu, S. Dolder, E. B. Rusanov, H. Stoecki-Evans, S. Decurtins, *C. R. Chim.* **2003**, *6*, 657; c) S.-X. Liu, S. Dolder, M. Pilkington, S. Decurtins, *J. Org. Chem.* **2002**, *67*, 3160; d) C. Jia, D. Zhang, Y. Xu, W. Xu, U. Hu, D. Zhu, *Synth. Met.* **2003**, *132*, 249; e) J. Becher, A. Hazell, C. J. McKenzie, C. Vestergaard, *Polyhedron* **2000**, *19*, 665; f) T. Devic, N. Avarvari, P. Batail, *Chem. Eur. J.* **2004**, *10*, 3697; g) A. Ota, L. Ouahab, S. Golhen, O. Cador, Y. Yoshida, G. Saito, *New J. Chem.* **2005**, *29*, 1135; h) S.-X. Liu, S. Dolder, P. Franz, A. Neels, H. Stoeckli-Evans, S. Decurtins, *Inorg. Chem.* **2003**, *42*, 4801; i) H. Xue, X.-J. Tang, L.-Z. Wu, L.-P. Zhang, C.-H. Tung, *J. Org. Chem.* **2005**, *70*, 9727; j) N. Benbellat, Y. Le Gal, S. Golhen, A. Gouasmia, L. Ouahab, J.-M. Fabre, *Eur. J. Org. Chem.* **2006**, 4237; k) K. Hervé, S.-X. Liu, O. Cador, S. Golhen, Y. Le Gal, A. Bousseksou, H. Stoeckli-Evans, S. Decurtins, L. Ouahab, *Eur. J. Inorg. Chem.* **2006**, 3498; l) J. Massue, N. Bellec, S. Chopin, E. Levillain, T. Roisnel, R. Clérac, D. Lorcy, *Inorg. Chem.* **2005**, *44*, 8740; m) P. Pellon, G. Gachot, J. Le Bris, S. Marchin, R. Carlier, D. Lorcy, *Inorg. Chem.* **2003**, *42*, 2056; n) B. W. Smucker, K. R. J. Dunbar, *J. Chem. Soc. Dalton Trans.* **2000**, 1309; o) T. Devic, P. Batail, M. Fourmigué, N. Avarvari, *Inorg. Chem.* **2004**, *43*, 3136; p) N. Avarvari, M. Fourmigué, *Chem. Commun.* **2004**, 1300; q) F. Iwahori, S. Golhen, L. Ouahab, R. Carlier, J.-P. Sutter, *Inorg. Chem.* **2001**, *40*, 6541; r) L. Ouahab, F. Iwahori, S. Golhen, R. Carlier, J.-P. Sutter, *Synth. Met.* **2003**, *133–134*, 505; s) C. Jia, S.-X. Liu, C. Ambrus, A. Neels, G. Labat, S. Decurtins, *Inorg. Chem.* **2006**, *45*, 3152; t) S. Ichikawa, S. Kimura, H. Mori, G. Yoshida, H. Tajima, *Inorg. Chem.* **2006**, *45*, 7575; u) L. Wang, B. Zhang, J. Zhang, *Inorg. Chem.* **2006**, *45*, 6860; v) K. S. Gavrilenko, Y. Le Gal, O. Cador, S. Golhen, L. Ouahab, *Chem. Commun.* **2007**, 280; w) G. Cosquer, F. Pointillart, Y. Le Gal; S. Golhen, O. Cador, L. Ouahab, *Inorg. Chem.* **2008**, *47*, 9730, S. Golhen, O. Cador, L. Ouahab, *Dalton Trans.* **2009**, 3495; x) F. Pointillart, Y. Le Gal; S. Golhen, O. Cador, L. Ouahab, *Inorg. Chem.* **2008**, *47*, 9730; y) Y. Umezono, W. Fujita, K. Awaga, *J. Am. Chem. Soc.* **2006**, *128*, 1084; z) F. Setifi, L. Ouahab, S. Golhen, Y. Yoshida, G. Saito, *Inorg. Chem.* **2003**, *42*, 1791; aa) K. Hervé, Y. Le Gal, L. Ouahab, S. Golhen, O. Cador, *Synth. Met.* **2005**, *153*, 461.

[4] a) T. Imakubo, H. Sawa, H. Tajima, R. Kato, *Synth. Met.* **1997**, *86*, 2047; b) M. Tamura, F. Matsuzaki, Y. Nishio, K. Kajita, T. Kitazawa, H. Mori, S. Tanaka, *Synth. Met.* **1999**, *102*, 1716; c) O. A. Dyachenko, O. N. Kazheva, V. V. Gritsenko, N. D. Kushch, *Synth. Met.* **2001**, *120*, 1017; d) T. Otsuka, H. Cui, A. Kobayashi, Y. Misaki, H. Kobayashi, *J. Solid State Chem.* **2002**, *168*, 444; e) N. D. Kushch, O. N. Kazheva, V. V. Gritsenko, L. I. Buravov, K. V. Van, O. A. Dyachenko, *Synth. Met.* **2001**, *123*, 171; f) M. Tamura, K. Yamanaka, Y. Mori, Y. Nishio, K. Kajita, H. Mori, S. Tanaka, J.-I. Yamaura, T. Imakubo, R. Kato, Y. Misaki, K. Tanaka, *Synth. Met.* **2001**, *120*, 1041; g) F. Pointillart, O. Maury, Y. Le Gal, S. Golhen, O. Cador, L. Ouahab, *Inorg. Chem.* **2009**, *48*, 7421; h) F. Pointillart, Y. Le Gal, S. Golhen, O. Cador, L. Ouahab, *Chem. Commun.* **2009**, 3777.

[5] R. L. Carlin, *Magnetochemistry*, Springer, Berlin **1986**.

[6] For example: a) N. Ishikawa, M. Sugita, T. Ishikawa, S. Koshihara, Y. Kaizu, *J. Am. Chem. Soc.* **2003**, *125*, 8694; b) N. Ishikawa, M. Sugita, W. Wernsdorfer, *J. Am. Chem. Soc.* **2005**, *127*, 3650; c) J. Tang, I. Hewitt, N. T. Madhu, G. Chastanet, W. Wernsdorfer, C. E. Anson, C. Benelli, R. Sessoli, A. K. Powell, *Angew. Chem.* **2006**, *118*, 1761; *Angew. Chem. Int. Ed.* **2006**, *45*, 1729; d) P.-H. Lin, T.-J. Burchell, R. Clérac, M. Murugesu, *Angew. Chem.* **2008**, *120*, 8980; *Angew. Chem. Int. Ed.* **2008**, *47*, 8848; e) N. Ishikawa, *Polyhedron* **2007**, *26*, 2147, and references herein; f) N. Ishikawa, M. Sugita, W. Wernsdorfer, *Angew. Chem.* **2005**, *117*, 2991; *Angew. Chem. Int. Ed.* **2005**, *44*, 2931; g) F. Cinti, A. Rettori, M. G. Pini, M. Mariani, E. Micotti, A. Lascialfari, N. Papinutto, A. Amato, A. Caneschi, D. Gatteschi, M. Affronte, *Phys. Rev. Lett.* **2008**, *100*, 057203; h) Z. Chen, B. Zhao, P. Cheng, X.-Q. Zhao, W. Shi, Y. Song, *Inorg. Chem.* **2009**, *48*, 3493.

[7] a) N. Sabbatini, M. Guardigli, I. Manet, *Handbook of the Physics and Chemistry of Rare Earths, Vol. 23*, Elsevier, Amsterdam, **1996**, p. 69; b) S. Comby, J.-C. G. Bünzli, *Handbook on the Physics and Chemistry of Rare Earths, Vol. 37*, Elsevier, Amsterdam, **2007**; Chapter 235.

[8] a) D. Parker, *Coord. Chem. Rev.* **2000**, *205*, 109; b) D. Parker, *Chem. Soc. Rev.* **2004**, *33*, 156; c) J.-C. G. Bünzli, C. Piguet, *Coord. Chem. Rev.* **2005**, *34*, 1048; d) S. V. Eliseeva, J.-C. G. Bünzli, *Coord. Chem. Rev.* **2010**, *39*, 189, and references therein.

[9] A. Lempicki, H. Samelson, *Phys. Lett.* **1963**, *4*, 133.

[10] a) A. de Bettencourt-Diaz, *Dalton Trans.* **2007**, 2229–2241; b) J. Kido, Y. Okamota, *Chem. Rev.* **2002**, *102*, 2357.

[11] J. H. Burroughes, D. D. C. Bradley, A. B. Holmes, *Nature* **1990**, *347*, 539.

[12] S. Faulkner, S. J. A. Pope, B. P. Burton-Pye, *Appl. Spectrosc. Rev.* **2004**, *39*, 1.

[13] a) M. H. V. Werts, M. A. Duin, J. W. Hofstraat, J. W. Verhoeven, *Chem. Commun.* **1999**, 799; b) Y. H. Kim, N. S. Baek, H. K. Kim, *ChemPhysChem* **2006**, *7*, 213; c) C. Yang, L.-M. Fu, Y. Wang, J.-P. Zhang, W.-P. Wong, X.-C. Ai, Y. F. Qiao, B.-S. Zou, L.-L. Gui, *Angew. Chem.* **2004**, *116*, 5120; *Angew. Chem. Int. Ed.* **2004**, *43*, 5010; d) A. D'Aleo, P. Picot, A. Beeby, J. A. G. Williams, B. Le Guennic, C. Andraud, O. Maury, *Inorg. Chem.* **2008**, *47*, 10258.

[14] a) T. Gunnlaugsson, F. Stomeo, *Org. Biomol. Chem.* **2007**, *5*, 1999; b) M. D. Ward, *Coord. Chem. Rev.* **2007**, *251*, 1663; c) D. Sénéchal, S. J. A. Pope, S. Quinn, S. Faulkner, T. Gunnlaugsson, *Inorg. Chem.* **2006**, *45*, 10040; d) S. G. Baca, H. Adams, D. Sykes, S. Faulkner, M. D. Ward, *Dalton Trans.* **2007**, 2419; e) P. Coppo, M. Duati, V. N. Kozhevnikov, J. W. Hofstraat, L. De Cola, *Angew. Chem.* **2005**, *117*, 1840; *Angew. Chem. Int. Ed.* **2005**, *44*, 1806; f) N. M. Shavaleev, L. P. Morrecraft, S. J. A. Pope, Z. R. Bell, S. Faulkner, M. D. Ward, *Chem. Eur. J.* **2003**, *9*, 5283; g) F. Kennedy, N. M. Shavaleev, T. Koullourou, Z. Bell, J. C. Jeffery, S. Faulkner, M. D. Ward, *Dalton Trans.* **2007**, 1492.

[15] a) C. Andraud, O. Maury, *Eur. J. Inorg. Chem.* **2009**, 4357; b) K.-L. Wong, W.-M. Kwok, W.-T. Wong, D. L. Phillips, K. W. Cheah, *Angew. Chem.* **2004**, *116*, 4759; *Angew. Chem. Int. Ed.* **2004**, *43*, 4659; c) L.-M. Fu, X.-F. Wen, X.-C. Ai, Y. Sun, Y.-S. Wu, J.-P. Zhang, Y. Wang, *Angew. Chem.* **2005**, *117*, 757; *Angew. Chem. Int. Ed.* **2005**, *44*, 747; d) R. Hao, M. Li, Y. Wang, J. Zhang, Y. Ma, L. Fu, X. Wen, Y. Wu, X. Ai, S. Zhang, Y. Wei, *Adv. Funct. Mater.* **2007**, *17*, 3663; e) A. D'Aléo, G. Pompidor, B. Elena, J. Vicat, P. L. Baldeck, L. Toupet, R. Kahn, C. Andraud, O. Maury, *ChemPhysChem* **2007**, *8*, 2125; f) X. Wen, M. Li, Y. Wang, J. Zhang, L. Fu, R. Hao, Y. Ma, X. Ai, *Langmuir* **2008**, *24*, 6932; g) A. D'Aleo, P. Picot, P. L. Baldeck, C. Andraud, O. Maury, *Inorg. Chem.* **2008**, *47*, 10269.

[16] C. C. Beedle, C. J. Stephenson, K. J. Heroux, W. Wernsdorfer, D. N. Hendrickson, *Inorg. Chem.* **2008**, *47*, 10798.

[17] a) M. H. Jo, J. E. Grose, K. Baheti, M. M. Deshmukh, J. J. Sokol, E. M. Rumberger, D. N. Hendrickson, J. R. Long, H. Park, D. C. Ralph, *Nano Lett.* **2006**, *6*, 2014; b) C. Ni, S. Shah, D. Hendrickson,

P. R. Bandaru, *Appl. Phys. Lett.* **2006**, *89*, 212104; c) L. Bogani, W. Wernsdorfer, *Nat. Mater.* **2008**, *7*, 179; d) E. Coronado, C. Marti-Gastaldo, S. Tatay, *Appl. Surf. Sci.* **2007**, *254*, 225; e) A. N. Abdi, J. P. Bucher, P. Rabu, O. Toulemonde, M. Drillon, P. Gerbier, *J. Appl. Phys.* **2004**, *95*, 7345.

[18] a) S. Faulkner, B. P. Burton-Pye, T. Khan, L. R. Martin, S. D. Wray, P. J. Skabara, *Chem. Commun.* **2002**, 1668; b) S. J. A. Pope, B. P. Burton-Pye, R. Berridge, T. Khan, P. Skabara, S. Faulkner, *Dalton Trans.* **2006**, 2907.

[19] F. Pointillart, Y. Le Gal, S. Golhen, O. Cador, L. Ouahab, *Inorg. Chem.* **2009**, *48*, 4631.

[20] F. Pointillart, T. Cauchy, Y. Le Gal, S. Golhen, O. Cador, L. Ouahab, *Inorg. Chem.* **2010**, *49*, 1947.

[21] a) V. S. Sastri, J. R. Perumareddi, V. Ramachandra Rao, G. V. S. Rayudu, J.-C. Bünzli, *Modern Aspects of Rare Earths and their Complexes*, Elsevier, Amsterdam, **2003**; b) K. Dehnicke, A. Greiner, *Angew. Chem.* **2003**, *115*, 1378; *Angew. Chem. Int. Ed.* **2003**, *42*, 1340; c) J. H. Forsberg, *Coord. Chem. Rev.* **1973**, *10*, 195.

[22] P. Maldivi, L. Petit, C. Adamo, V. Vetere, *C. R. Chim.* **2007**, *10*, 888.

[23] J. I. Bruce, R. S. Dickins, L. J. Govenlock, T. Gunnlaugsson, S. Lopinski, M. P. Lowe, D. Parker, R. D. Peacock, J. J. B. Perry, S. Aime, M. Botta, *J. Am. Chem. Soc.* **2000**, *122*, 9674.

[24] L. Di Bari, G. Pintacuda, P. Salvadori, R. S. Dickins, D. Parker, *J. Am. Chem. Soc.* **2000**, *122*, 9257.

[25] N. Tancrez, C. Feuvrie, I. Ledoux, J. Zyss, L. Toupet, H. Le Bozec, O. Maury, *J. Am. Chem. Soc.* **2005**, *127*, 13474.

[26] E. Furet, K. Costuas, P. Rabiller, O. Maury, *J. Am. Chem. Soc.* **2008**, *130*, 2180.

[27] R. D. Shannon, *Acta Crystallogr. Sect. A* **1976**, *32*, 751.

[28] a) D. R. van Staveren, G. A. vanAlbada, J. G. Haasnoot, H. Kooijman, M. Manotti, A. Lanfredi, P. J. Nieuwenhuizen, A. L. Spek, F. Ugozzoli, I. T. Weyherm, J. Reedijk, *Inorg. Chim. Acta* **2001**, *315*, 163; b) G. Klopman, *J. Am. Chem. Soc.* **1968**, *90*, 223.

[29] C. Benelli, D. Gatteschi, *Chem. Rev.* **2002**, *102*, 2369, and references therein.

[30] R. B. King, *J. Am. Chem. Soc.* **1969**, *91*, 7211.

[31] S. V. Eliseeva, M. Ryazanov, F. Gumy, S. I. Troyanov, L. S. Lepnev, J.-C. G. Bünzli, N. P. Kuzmina, *Eur. J. Inorg. Chem.* **2006**, 4809.

[32] a) E. L. Muetterties, L. J. Guggenberger, *J. Am. Chem. Soc.* **1974**, *96*, 1748; b) M. G. B. Drew, *Coord. Chem. Rev.* **1977**, *24*, 179.

[33] O. Kahn, *Molecular Magnetism*, VCH, Weinheim, **1993**.

[34] J.-P. Sutter, M. L. Kahn, *Magnetism: Molecules to Materials V*, VCH, Weinheim, **2005**.

[35] a) M. L. Kahn, C. Mathonière, O. Kahn, *Inorg. Chem.* **1999**, *38*, 3692; b) J.-P. Costes, F. Dahan, A. Dupuis, J.-P. Laurent, *Chem. Eur. J.* **1998**, *4*, 1616; c) E. A. Boudreaux, L. N. Mulay, *Theory and Applications of Molecular Paramagnetism*, Wiley, New York, **1976**; d) A. Herpin, *Théorie du Magnétisme*, Press. Univ. France, Paris, **1968**; e) J.-P. Sutter, M. L. Kahn, O. Kahn, *Adv. Mater.* **1999**, *11*, 863; f) M. L. Kahn, M. L. P. Lecante, M. Verelst, C. Mathonière, O. Kahn, *Chem. Mater.* **2000**, *12*, 3073; g) T. Kido, Y. Ikuta, Y. Sunatsuki, Y. Ogawa, N. Matsumoto, *Inorg. Chem.* **2003**, *42*, 398; h) A. Caneschi, A. Dei, D. Gatteschi, S. Poussereau, L. Sorace, *Dalton Trans.* **2004**, 1048; i) R. Koner, H.-H. Lin, H.-H. Wie, S. Mohanta, *Inorg. Chem.* **2005**, *44*, 3524.

[36] M. L. Kahn, R. Ballou, P. Porcher, O. Kahn, J.-P. Sutter, *Chem. Eur. J.* **2002**, *8*, 525.

[37] P. Porcher, M. C. Dos Santos, O. Malta, *Phys. Chem. Chem. Phys.* **1999**, *1*, 397.

[38] J. C. Bünzli in *Lanthanide Probes in Life, Chemicals and Earth Sciences: Theory and Practice* (Eds.: J. C. G. Bünzli, G. R. Chopin), Elsevier, Amsterdam, **1989**, p. 219.

[39] a) A. Panagiotopoulos, T. F. Zafiropoulos, S. P. Perlepes, E. Bakalbassis, I. Masson-Ramade, O. Kahn, A. Terzis, C. P. Raptopoulou, *Inorg. Chem.* **1995**, *34*, 4918; b) F. Avecilla, C. Platas-Iglesias, R. Rodriguez-Cortinas, G. Guillemot, J.-C. G. Bünzli, C. D. Brondino, C. F. G. C. Geraldes, A. De Blas, T. Rodriguez-Blas, *Dalton Trans.* **2002**, 4658.

[40] J. D. Rinehart, T. D. Harris, S. A. Kozimor, B. M. Bartlett, J. R. Long, *Inorg. Chem.* **2009**, *48*, 3382.

[41] C. Jia, S.-X. Liu, C. Tanner, C. Leiggener, A. Neels, L. Sanguinet, E. Levillain, S. Leutwyler, A. Hauser, S. Decurstins, *Cent. Eur. J. Chem.* **2007**, *13*, 3804.

[42] a) D. Sénéchal, A. Hemeryck, N. Tancrez, L. Toupet, J. A. G. Williams, I. Ledoux, J. Zyss, A. Boucekkine, J.-P. Guégan, H. Le Bozec, O. Maury, *J. Am. Chem. Soc.* **2006**, *128*, 12243; b) B. Wang, M. R. Wasielewski, *J. Am. Chem. Soc.* **1997**, *119*, 12; c) D. Sénéchal, L. Toupet, I. Ledoux, J. Zyss, H. Le Bozec, O. Maury, *Chem. Commun.* **2004**, 2180.

[43] C. Goze, N. Dupont, E. Beitler, C. Leiggener, H. Jia, P. Monbaron, S.-X. Liu, A. Neels, A. Hauser, S. Decurtins, *Inorg. Chem.* **2008**, *47*, 11010.

[44] a) W. Huang, D. Wu, D. Guo, X. Zhu, C. He, Q. Meng, C. Duan, *Dalton Trans.* **2009**, 2081; b) G. A. Hebbink, L. Grave, L. A. Woldering, D. N. Reinhoudt, F. C. J. M. van Veggel, *J. Phys. Chem. A* **2003**, *107*, 2483; c) M. H. V. Werts, J. W. Hofstraat, F. A. J. Geurts, J. W. Verhoeven, *Chem. Phys. Lett.* **1997**, *276*, 196.

[45] R. Ziessel, G. Ulrich, L. Charbonnière, D. Imbert, R. Scopelliti, J.-C. G. Bünzli, *Chem. Eur. J.* **2006**, *12*, 5060.

[46] N. M. Shavaleev, R. Scopelliti, F. Gumy, J.-C. G. Bünzli, *Eur. J. Inorg. Chem.* **2008**, 1523.

[47] a) W. D. Horrocks, Jr., J. P. Bolender, W. D. Smith, R. M. Supkowski, *J. Am. Chem. Soc.* **1997**, *119*, 5972; b) R. M. Supkowski, J. P. Bolender, W. D. Smith, L. E. L. Reynolds, W. D. Horrocks, Jr., *Coord. Chem. Rev.* **1999**, *185–186*, 307.

[48] a) A. Beeby, S. Faulkner, J. A. G. Williams, *Dalton Trans.* **2002**, 1918; b) T. Lazarides, M. A. H. Alamiry, H. Adams, S. J. A. Pope, S. Faulkner, J. A. Weinstein, M. D. Ward, *Dalton Trans.* **2007**, 1484; c) T. Lazarides, N. M. Tart, D. Sykes, S. Faulkner, A. Barbieri, M. D. Ward, *Dalton Trans.* **2009**, 3971.

[49] D. Rehm A. Weller, *Isr. J. Chem.* **1970**, *10*, 259.

[50] M. F. Richardson, W. F. Wagner, D. E. Sands, *J. Inorg. Nucl. Chem.* **1968**, *30*, 1275.

[51] Z. Otwinowski, W. Minor, *Processing of X-ray Diffraction Data Collected in Oscillation Mode in Methods in Enzymology, Vol. 276: Macromolecular Crystallography, Part A* (Eds.: C. W. Carter, R. M. Sweet, Jr.), Academic Press, New York, **1997**, pp. 307–326.

[52] a) J. P. Perdew, K. Burke, M. Ernzerhof, *Phys. Rev. Lett.* **1996**, *77*, 3865; b) C. Adamo, V. Barone, *J. Chem. Phys.* **1999**, *110*, 6158.

[53] Gaussian 03, Revision D.02, M. J. Frisch, G. W. Trucks, H. B. Schlegel, G. E. Scuseria, M. A. Robb, J. R. Cheeseman, J. A. Montgomery, Jr., T. Vreven, K. N. Kudin, J. C. Burant, J. M. Millam, S. S. Iyengar, J. Tomasi, V. Barone, B. Mennucci, M. Cossi, G. Scalmani, N. Rega, G. A. Petersson, H. Nakatsuji, M. Hada, M. Ehara, K. Toyota, R. Fukuda, J. Hasegawa, M. Ishida, T. Nakajima, Y. Honda, O. Kitao, H. Nakai, M. Klene, X. Li, J. E. Knox, H. P. Hratchian, J. B. Cross, V. Bakken, C. Adamo, J. Jaramillo, R. Gomperts, R. E. Stratmann, O. Yazyev, A. J. Austin, R. Cammi, C. Pomelli, J. W. Ochterski, P. Y. Ayala, K. Morokuma, G. A. Voth, P. Salvador, J. J. Dannenberg, V. G. Zakrzewski, S. Dapprich, A. D. Daniels, M. C. Strain, O. Farkas, D. K. Malick, A. D. Rabuck, K. Raghavachari, J. B. Foresman, J. V. Ortiz, Q. Cui, A. G. Baboul, S. Clifford, J. Cioslowski, B. B. Stefanov, G. Liu, A. Liashenko, P. Piskorz, I. Komaromi, R. L. Martin, D. J. Fox, T. Keith, M. A. Al-Laham, C. Y. Peng, A. Nanayakkara, M. Challacombe, P. M. W. Gill, B. Johnson, W. Chen, M. W. Wong, C. Gonzalez, J. A. Pople, Gaussian, Inc., Pittsburgh, **2003**.

[54] a) A. D. Becke, *Phys. Rev. A* **1988**, *38*, 3098; b) J. P. Perdew, *Phys. Rev. B* **1986**, *33*, 8822.

[55] F. Weigend, R. Ahlrichs, *Phys. Chem. Chem. Phys.* **2005**, *7*, 3297.

Received: May 25, 2010
Published online: September 8, 2010

